Fully Controllable Design and Fabrication of Three-Dimensional Lattice Supercapacitors

Jian Song*, Yuejiao Chen, Ke Cao, Yang Lu, John H. Xin, and Xiaoming Tao*

Jian Song - College of Civil Engineering, Shenzhen University, Shenzhen 518000, China; Nanotechnology Center of Functional and Intelligent Textiles and Apparel, Institute of Textiles and Clothing, The Hong Kong Polytechnic University, Hong Kong 999077, China; http://orcid.org/0000-0001-8502-157X; Email: dfsongjian2006@126.com

Xiaoming Tao - Nanotechnology Center of Functional and Intelligent Textiles and Apparel, Institute of Textiles and Clothing, The Hong Kong Polytechnic University, Hong Kong 999077, China; Email: taoxiaoming@polyu.edu.hk

Yuejiao Chen - Nanotechnology Center of Functional and Intelligent Textiles and Apparel, Institute of Textiles and Clothing, The Hong Kong Polytechnic University, Hong Kong 999077, China; State Key Laboratory of Powder Metallurgy, Central South University, Changsha 410083, China

Ke Cao - Department of Mechanical and Biomedical Engineering, City University of Hong Kong, 83 Tat Chee Avenue, Kowloon, Hong Kong 999077, China

Yang Lu - Department of Mechanical and Biomedical Engineering, City University of Hong Kong, 83 Tat Chee Avenue, Kowloon, Hong Kong 999077, China

John H. Xin - Nanotechnology Center of Functional and Intelligent Textiles and Apparel, Institute of Textiles and Clothing, The Hong Kong Polytechnic University, Hong Kong 999077, China

Abstract

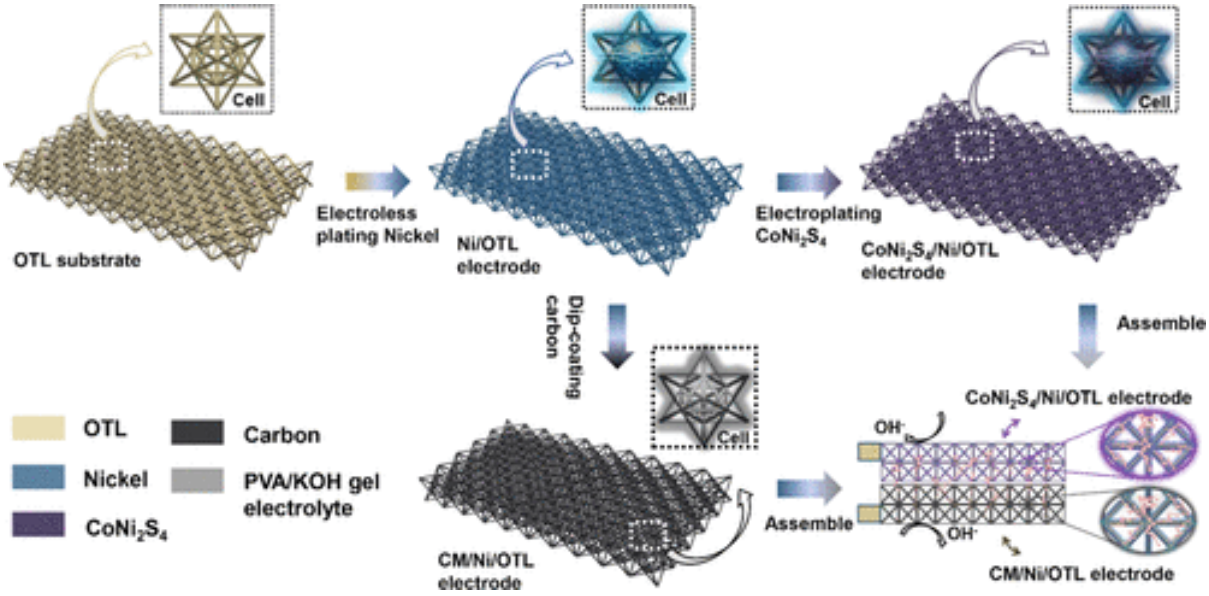

Supercapacitors have been proven to be a superior candidate for energy storage systems. Yet, most of them are of an approximately two-dimensional structure, without taking full advantage of the spatial superiority to load more mass of active materials. Moreover, three-dimensional (3D) sponge electrodes may hinder ion transmission due to the significant variations in porous structures. In this work, fully controllable 3D lattice supercapacitors with the ordered porous structures were fabricated for the first time via using 3D printing technology. To increase the mass loading capacity, active materials, including metal films, carbon nanomaterials, and transition-metal sulfides, were hierarchically loaded onto the surface of the lattice substrate by using electroless plating, dip-coating, and electrodeposition methods. The as-fabricated $CoNi_2S_4$/Ni/octet-truss lattice (OTL) electrode demonstrates a high capacitance until up to 1216 F g^{-1} (KOH electrolyte). The lattice asymmetric all-solid-state supercapacitors, composed of $CoNi_2S_4$/Ni/OTL as anode and carbon materials/Ni/OTL as cathode, display the highest specific capacitance of 23.5 F g^{-1}, a 10.6 Wh kg^{-1} energy density at the 2488.3 W kg^{-1} power density, and a robustness (77.3% capacitance retention after 1800 cycles). We expect that the design and fabrication method for the fully controllable 3D lattice supercapacitor with hierarchical activating materials can open a door to develop 3D supercapacitors.

KEYWORDS: 3D printing technology, lattice electrodes, ravinelike $CoNi_2S_4$, carbon materials, supercapacitors

1. Introduction

Nowadays, electric vehicles, smartphones, and Internet-of-Things have demanded rapid development of high-performance electric power sources that can continuously provide clean

energy with the rapid charge–discharge response. (1,2) From this viewpoint, supercapacitors with a fast charge–discharge response, good cycling stability, superior power density, and environmental friendliness are of interest as energy storage systems. (3−5) Up to now, the power densities and lifespan of supercapacitors have excessed 10 kW kg^{-1} and 10^5 cycles, respectively. (6,7) Compared with the conventional Li-ion batteries, supercapacitors have many advantages, viz., very high rates of charge and discharge, good reversibility, and high cycle efficiency. However, low energy density and large energy dissipation compared to those of batteries are still major restrictive factors for practical applications of supercapacitors. Increase of mass loading by electrodes promises an available route to improve the supercapacitors' energy density, i.e., thick sponge electrodes to enhance the mass loading. Furthermore, the power density is generally determined by the electron/ion transmission efficiency. Thick electrodes with good mass loading capacity may hinder ion transmission induced by varying internal architectures, thus resulting in energy dissipation. (8)

The utilization of a 3D framework with porous architecture as an electrode may meet this challenge of competing mechanisms to assemble supercapacitors that can effectively facilitate the electron/ion transmission, due to the merit of porous distribution in 3D space. One-dimensional (1D) fiber yarns (9) and two-dimensional (2D) nonwoven fabric (10,11) as substrates of electrodes have been widely investigated since they are commercially available, extensively retrievable, and electrochemically stability. However, if the active materials only distribute in 1D and 2D space, to some degree, the further improvement of energy density of a supercapacitor is limited. Additionally, nickel foam with an open-cell architecture is generally used as an electrode (1) but it is commonly difficult to precisely control the pore structure and size in practical applications. To utilize the 3D space, a few 3D materials, i.e., sponge (12,13) and natural wood materials, (14) were adopted as the substrates of electrodes. Although they can indeed take advantage of 3D space where the electron/ion can transport along the spatial framework to fulfill the energy storage, the structural variations in microscale and disordered channels and pores reduce the transmission rate of charges. "Lattice structures" commonly regarded as reticulated and cellular structures composed of a multitude of repetitive cells that possess ordered structure and ultralow density may offer an alternative solution, especially facilitated by 3D printing technology. (15,16) Until now, to the best of our knowledge, few lattice structures have been designed for and used as open-cell porous electrodes.

In addition to the merit of a 3D space, it is effective to construct hierarchical structures to increase the mass loading capacity and further improve the energy density. An open-cell porous

electrode can simultaneously possess the pseudocapacitive and double-layer capacitive characteristics by loading hierarchical nanostructures onto 3D electrode, i.e., carbon nanotube, (17) graphene, (18) metal oxides (19)/sulfides, (20) etc. Among them, transition-metal sulfides, such as Ni_2S_3, (21) Co_3S_4, (22) and $CoNi_2S$, (23,24) have been recently reported as the effective pseudocapacitive activating materials because of better electrochemical performance as well as superior conductivity compared to that of the corresponding oxide. (25,26) Particularly, some sulfides with two metal components, i.e., cobalt and nickel elements, significantly attribute larger redox response in comparison with the sulfides with a single component, leading to higher energy density. (23,27,28) Nevertheless, it is still a great challenge to realize the fully controllable design from selecting/fabricating the 3D substrate structure to hierarchically loading active materials onto the substrate.

In this regard, a fully controllable design of a 3D lattice asymmetric supercapacitor was implemented for the first time. To overcome the shortage of ordered architecture in random porous substrates, 3D printing technology with a minimum characteristic length of 0.2 mm was successfully used to make an octet-truss lattice (OTL) substrate with ordered mesoporous characteristics, followed by an electroless plating process. Transition-metal sulfides with excellent pseudocapacitive performance were introduced by electrodeposition method as the active materials in the anode to form the hierarchical structure. On the other hand, MWCNT, graphene, acetylene black, and carboxyl methyl cellulose (CMC) were used to coat the surface of nickel film as the cathode. In addition, all fabrication processes were conducted at ambient conditions, viz., no elevated temperature, no annealing, and no hydrothermal treatment, which can ensure the stability of a photopolymer substrate. We demonstrate the supercapacitors with 3D OTL electrodes that can reach a maximum specific capacitance of 1216 F g^{-1} (KOH electrolyte). The lattice asymmetric all-solid-state supercapacitors (LASCs) exhibit a 10.6 Wh kg^{-1} energy density at the 2488 W kg^{-1} power density, as well as 77.3% capacitance retention after 1800 cycles.

2. Results and Discussion

2.1. Structural Characterization

2.1.1. Design and Fabrication of Lattice Supercapacitors on the Basis of 3D Printing Technology

We printed a set of three-dimensional-shaped and well-ordered octet-truss lattice (OTL) substrates and first adopted them as 3D electrodes in supercapacitors. OTL was reported to have an ordered 3D networklike structure and comprehensive characterization between tension-dominated and compression-dominated deformation. (29,30) In this work, OTL substrates were synthesized by using the projection stereolithography (SLA), in which photosensitive liquid resin was solidified by a UV laser (see Figure 1a). The detailed printing process can be seen in the Experimental Section.

Figure 1

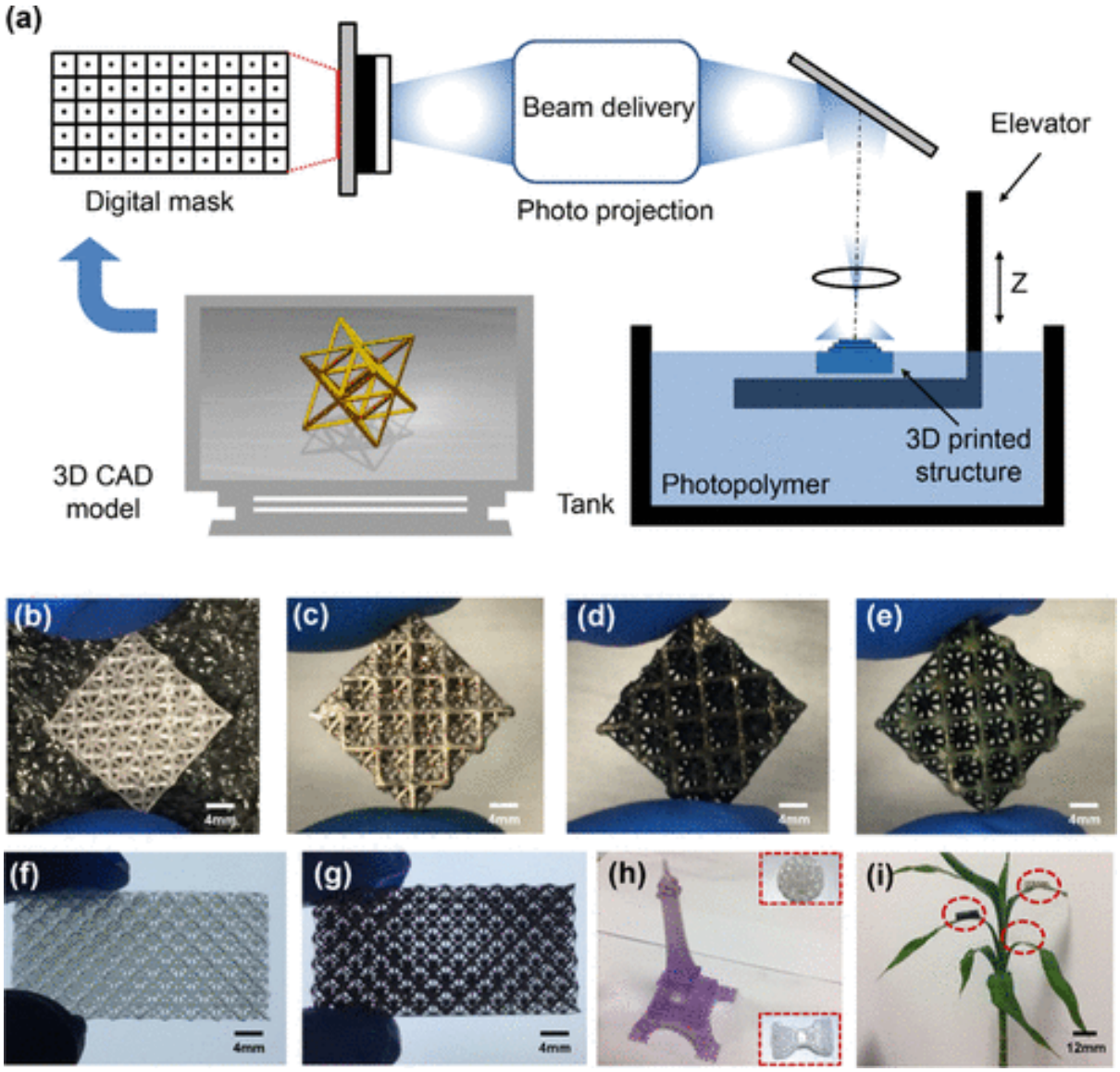

Figure 1. Fabrication process of ultralight and well-ordered lattice substrates and electrodes. (a) Schematic illustration of the SLA process where dynamic digital masks are projected into the photosensitive, layer-by-layer structures with a resolution of ~200 μm can be facilely fabricated. (b–e) OTL substrates with 3 × 3 × 1 cells, Ni/OTL electrode, $CoNi_2S_4$/Ni/OTL electrode, and CM/Ni/OTL electrode. (f, g) Another enlarged OTL substrate fabricated by 3D printing and Ni/OTL electrode. (h) 3D-printed Eiffel Tower with complex lattice structure. Inset images are the 3D-printed bowknot and hemisphere structures with porous characteristics. (i) Illustration of OTL, Ni/OTL, and CM/OTL electrodes located on the bamboo's leaves, indicating that ultralight 3D-printed electrodes were obtained.

The as-fabricated OTL substrate comprises 3 (length) × 3 (width) × 1 (thickness) cells, where each cell possesses an ordered octahedron as the core of OTL, surrounded by eight tetrahedra that are located on the six surfaces of OTL. Each node is directly connected by 36 identical solid rod trusses; see Figure 1b. The reason why we chose the OTL structure as the substrate is that the octa-truss structure not only possesses an excellent load-bearing capacity in comparison with the other structures, i.e., face-centered cubic (FCC)-like lattice and body-centered cubic (BCC)-like lattice substrates but also the internal eight trusses can serve as the transport routes of electrons/ions; see Figure S1, SI. Additionally, the finite element analyses based on the OTL, BCC-like, and FCC-like structures were carried out, which reveal the dominant deformation characteristics of each octa-truss under compressional load is stretching/compression rather than bending, giving an indication of high mechanical performance, i.e., the stiffness-to-weight ratio (Figure S2b–d, SI). (29,31,32) Furthermore, compared with the pure polymer OTL, the metal nickel film can effectively reduce the overall stress level of core polymer in the Ni-coated OTL (Figure S2e–g, SI).

Figure 1f–h also exhibits various lattice structures fabricated by 3D printing technology, indicating that the lattice structures can be facilely printed by using SLA. In addition, three lattice structures with ultralow density can stand upon the bamboo's leaves; see Figure 1i.

2.1.2. Material and Structural Characterizations

For the $CoNi_2S_4$/Ni/OTL anodes, the $CoNi_2S_4$ nanosheets were synthesized on the surface of Ni/OTL electrode by adopting a one-step potentiostatic electrodeposition method within 10, 15, and 20 min at ambient temperature, respectively. (33) The possible synthesis mechanism is explained as follows. The Co–Ni precursor was first grown on the surface of the nickel film in virtue of OH^- ions originating from the decomposition of H_2O in the anode. Afterward, the Co–Ni precursor can be immediately transformed into Co–Ni–S nanosheets with the help of substantial S^{2-} ions deriving from the NH_2CSNH_2 in solution, which can rapidly exchange with OH^- ions. Furthermore, the charge–discharge mechanism in $CoNi_2S_4$/Ni/OTL electrodes could be attributed such that after charging the supercapacitor, OH^- anions happen to the redox reactions with $CoNi_2S_4$, resulting in the generation of the Co/Ni–S–OH, whereas the backward reaction happens during the discharge process (Figure 2).

Figure 2

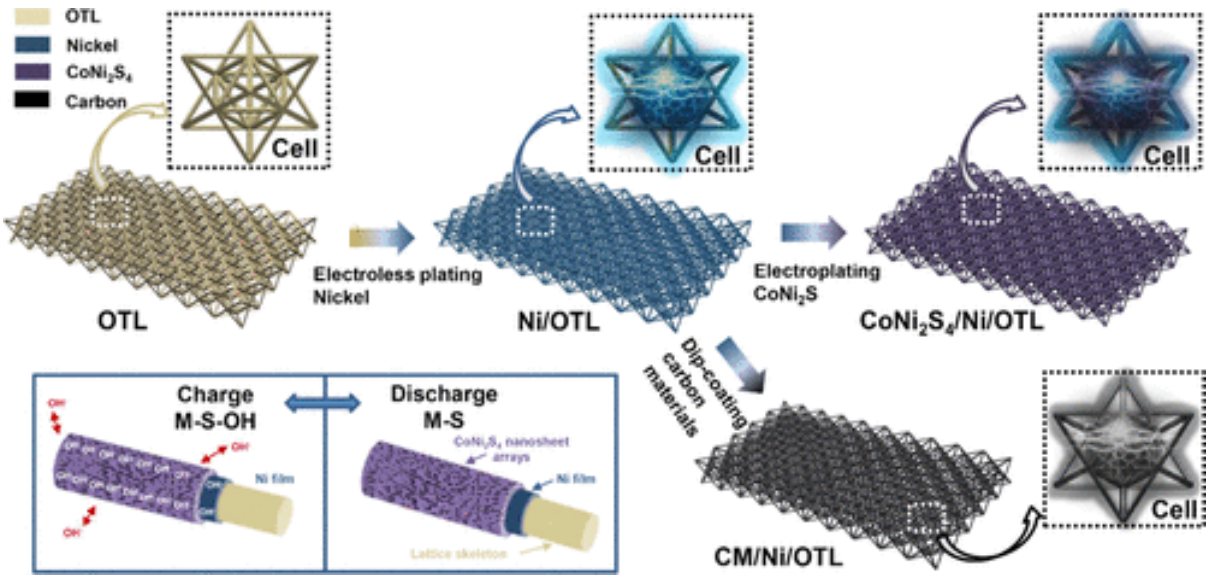

Figure 2. Schematic illustration of the fabricated 3D Ni/OTL, $CoNi_2S_4$/Ni/OTL, and CM/Ni/OTL electrodes; the inset shows the charge–discharge mechanism of the $CoNi_2S_4$/Ni/OTL anodes in the three-electrode system.

For the CM/Ni/OTL cathodes, a facile dip-coating method was used to coat carbon materials with various mass ratios of MWCNT and graphene on the surface of Ni/OTL electrode (Figure 2). Both the MWCNT and graphene possess an excellent double-layer capacitance characteristic, and the cross-linked routes formed by MWCNT are beneficial for the transportation of ions and electrons. (1) Thus, the CM/Ni/OTL electrodes were used as the cathodes in supercapacitors to further enlarge the voltage window.

Additionally, mechanical properties of the OTL substrate are important for application as the substrates of supercapacitor electrodes. Although it is difficult to realize a completely flexible 3D OTL substrate, like 2D textile or 3D sponge, we adopted three effective methods to enhance the flexibility of a 3D OTL substrate: (1) the ductile polymer was used as the photopolymer, which possesses a relatively low modulus of 240 MPa and high elastic–plastic deformation capacity of ~80% (see Figure 3a); (2) the struct diameter was controlled to 0.5 mm, which was enough slender to enhance the deformation capacity; (34) and (3) a net-shaped lattice structure enhanced the deformation capacity. (35)Figure 3b demonstrates the stress vs strain curves of OTL substrates. Young's moduli of OTL substrates were calculated according to the slope of the corresponding linear part, which are 17.4 and 17.3 MPa, respectively. With the increase of external load, the nonlinear behavior was found in the stress–strain curves, which is attributed

to the plastic deformation of the structs. Furthermore, the net-shaped characteristic of OTL substrates brings out a gradually damaged deformation behavior. Therefore, the OTL substrates possess a good deformation capacity; see Figure 3c.

Figure 3

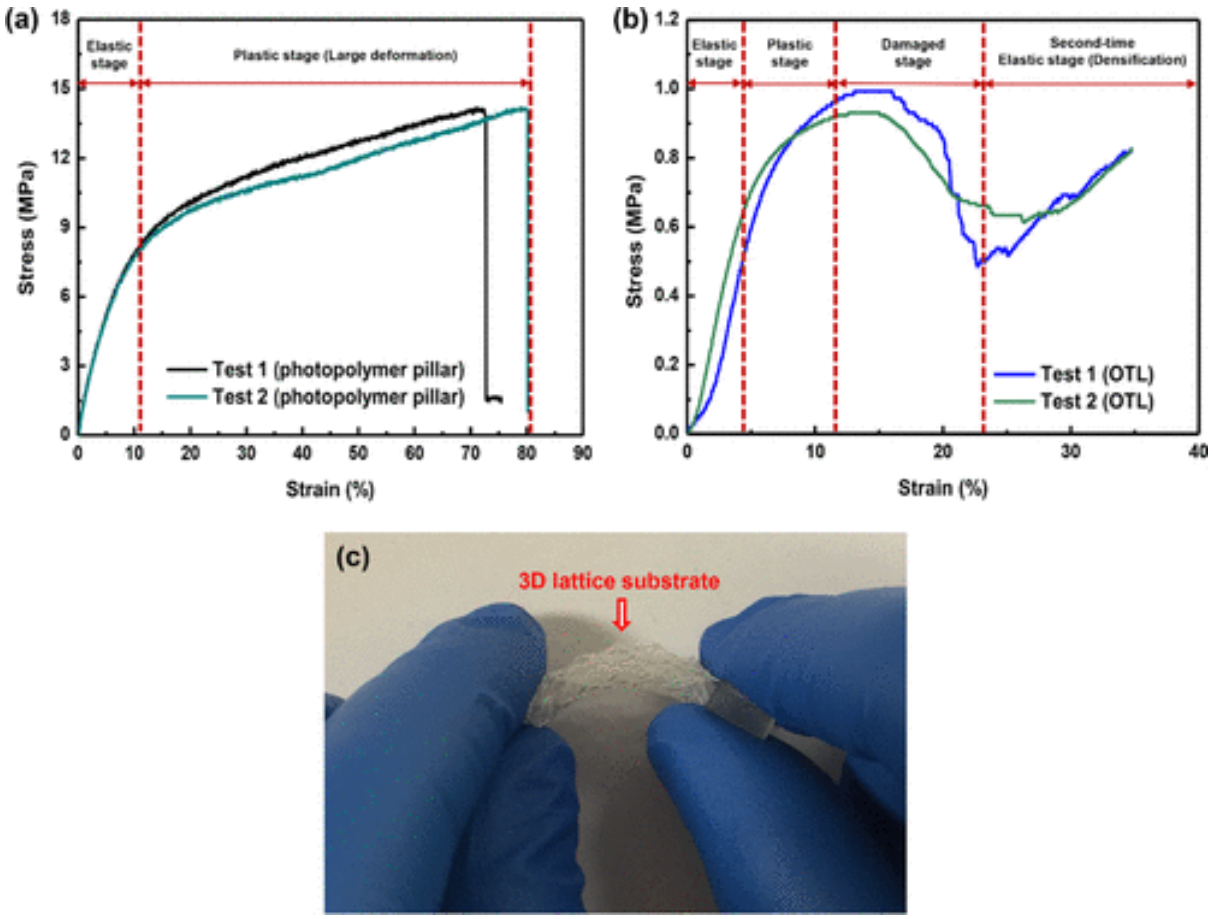

Figure 3. (a) Stress vs strain curves of photopolymer pillars; (b) stress vs strain curves of OTL substrates; and (c) the deformed OTL substrate.

Figure 4 depicts the morphology of the OTL, Ni/OTL, $CoNi_2S_4$/Ni/OTL, and CM/Ni/OTL electrodes. Obviously, the low-magnification SEM images from Figure 4a,e,i,m show that the nickel, $CoNi_2S_4$, and carbon nanomaterials (MWCNT, graphene) were uniformly covered on the polymer OTL substrate, respectively, completely maintaining the 3D framework of the substrate. To be more specific, Figure 4b exhibits the cascade-shaped structure that can be found in each inclined truss of OTL but in reality, the surfaces of the polymer framework present a certain extent of wrinkles, contributing to attachment of other active materials (Figure 4c,d). Through the electroless plating technology, wrinkled nickel film almost completely covered the OTL substrate (Figure 4f–h), which not only ensures the continuity of

conductive materials but also provides a uniform substrate for the sequential electrodeposition of $CoNi_2S_4$. Importantly, nonconductive 3D polymer lattices have been transferred into conductive 3D nickel@polymer lattices.

Figure 4

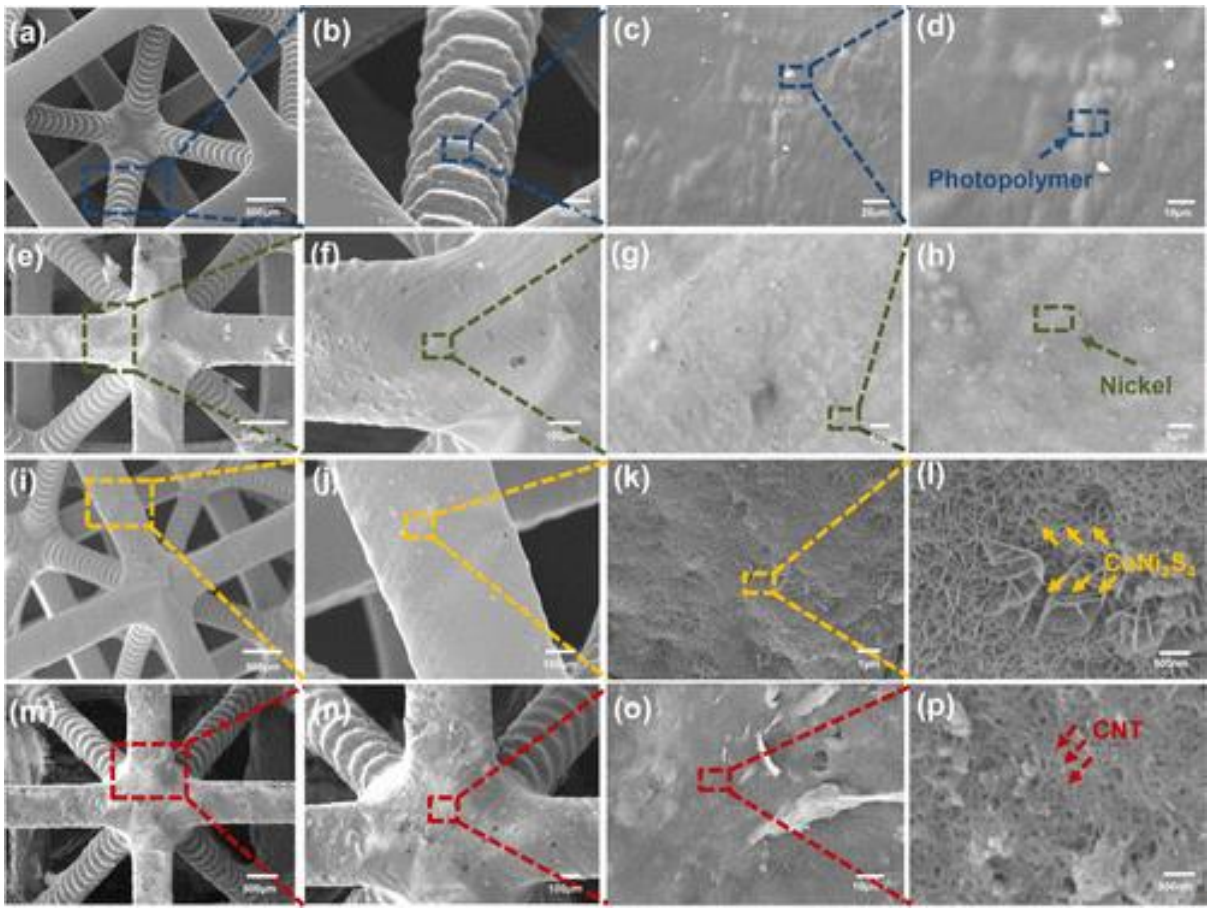

Figure 4. SEM images of lattice electrodes at different magnifications: (a–d) OTL substrate, (e–h) Ni/OTL electrode, (i–l) $CoNi_2S_4$/Ni/OTL electrode; and (m–p) CM/Ni/OTL electrode.

Additionally, the magnified SEM images in Figure 4k,l demonstrate that ravinelike Co–Ni sulfur nanosheets vertically generated on the surfaces of nickel film by the one-step electrodeposition. The formation of such ravinelike 3D structure could be ascribed to the etching-like effect by S^{2-} ions and the unequal diffusion of sulfur ions and cationic species. Obviously, this morphology will greatly enlarge the electrode–electrolyte contact area, which is beneficial to enhance the electrochemical performances. (23,36) Moreover, BET test demonstrates the pore size of electrodeposited $CoNi_2S_4$ powders shaved from the steel disk is mainly distributed near 1 nm, which to some degree suggests that the $CoNi_2S_4$ can provide more routes to transmit electrons/ions between electrolyte and hierarchical activate materials

in each area (Figure S6, SI). On the other hand, the dip-coating method ensures the carbon materials are composed of MWCNTs, graphene, and acetylene black uniformly coated on the surfaces of Ni/OTL electrode (Figure 4n,o). Nevertheless, from the high-magnification SEM image in Figure 4p, the carbon materials form a complex 3D network, efficiently enhancing the electrode/electrolyte contact area, which can also be verified by the BET test (Figure S6, SI). (37)

In brief, we successfully constructed the hierarchical structure on the 3D lattice electrodes by using 3D printing, electroless plating, and electrodeposition technologies, thus resulting in improving the mass loading capacity.

Figure 5 further illustrates the morphology of electroless plating metal film and $CoNi_2S_4$ powders peeled off from the electrodes via transmission electron microscopy (TEM). From Figure 5a, a large number of nanoscale particles (black sphere) disperse within the film. The electron diffraction pattern (Figure 5b) and X-ray diffraction (XRD) spectra (Figure S3a, SI) confirm that the synthesized film is a Ni–P alloy, in which the black particles represent nanocrystalline nickel, which are surrounded by shallow colored phosphor. Furthermore, coated nickel can effectively reduce the stress level of the core polymer in Ni/OTL electrode in comparison with the pure polymer OTL electrode (Figure S2, SI). These findings are also in reasonable agreement with previously reported work. (38) TEM image of $CoNi_2S_4$ nanosheets in Figure 5c demonstrates that the surface is densely wrinkled (black ribbon). Figure 5d illustrates a high-resolution TEM (HRTEM) image, in which the polycrystalline nature of $CoNi_2S_4$ nanosheets is observed, and the fringe spacings of 0.192, 0.236, and 0.284 nm can be ascribed to (422), (400), and (311) planes of $CoNi_2S_4$. Simultaneously, well-defined diffraction rings are observed by the selected area electron diffraction, which correspond to (311), (400), (422), and (440) planes of $CoNi_2S_4$. The compositional distributions of $CoNi_2S_4$ nanosheets are quantitatively identified by TEM-energy-dispersive X-ray (TEM-EDX) spectroscopy; see Figure 5e–h. The TEM-EDX spectroscopy presents that the Co, Ni, and S components coexist in the one-step-synthesized nanosheets. Furthermore, Figure 5i shows that the corresponding element ratio for Co, Ni, and S is about 1:1.84:3.5, which quite approaches the composition of $CoNi_2S_4$.

Figure 5

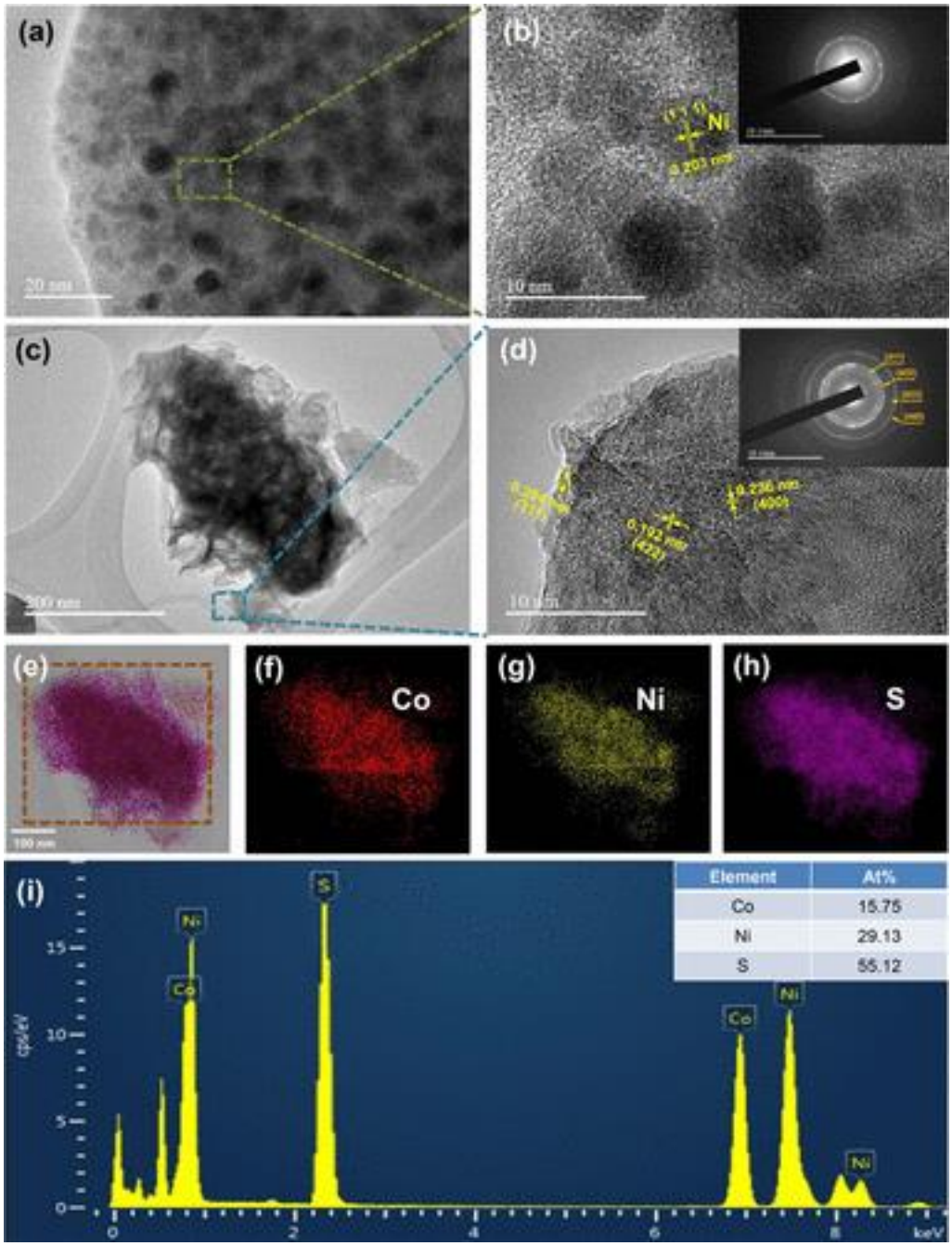

Figure 5. TEM and EDX spectroscopy images of electrode materials: (a, b) TEM and HRTEM images of nickel film; Inset: SAED pattern of nickel film. (c, d) TEM and HRTEM images of as-fabricated $CoNi_2S_4$; Inset: SAED pattern of $CoNi_2S_4$. (e–h) TEM-EDX spectroscopy of different elements Co, Ni, and S in the $CoNi_2S_4$. (i) The corresponding elemental contents in TEM-EDX spectroscopy of as-fabricated $CoNi_2S_4$ nanosheets.

Importantly, the one-step electrodeposition technique shows many advantages for the synthesis of $CoNi_2S_4$ nanosheets, such as facile technology and controllable conditions, especially at ambient temperature, which can effectively avoid damages to a polymer substrate compared with the high-temperature and high-pressure hydrothermal technique. (23,36,39)

In addition to the characterization of as-fabricated nickel film and Co–Ni sulfide nanosheets, Figure S4 exhibits TEM images of MWCNT and graphene. The fringe spacing of 0.34 nm for MWCNT and graphene confirms the co-existence of both MWCNT and graphene in the mixture of carbon materials.

Figure 6a exhibits the XRD patterns of $CoNi_2S_4$ nanosheets peeled off from the as-fabricated $CoNi_2S_4$/Ni/OTL electrodes. From analysis of the XRD patterns, the peaks of $CoNi_2S_4$ are relatively weak, which indicates the low crystallinity of one-step synthesized $CoNi_2S_4$ nanosheets. Four representative peaks at 31.4, 38.2, 50.1, and 55.1° can completely correspond to the (311), (400), (511), and (440) diffraction planes of the cubic $CoNi_2S_4$ (JCPDS No. 24-0334), respectively, confirming that the $CoNi_2S_4$ nanosheets were successfully fabricated, where the peaks marked with asterisks originate from the nickel film. This result also agrees with the report about the $CoNi_2S_4$ phase fabricated by using hydrothermal method, (40) which indicates the proposed one-step electrochemical deposition method is an effective route to fabricate the $CoNi_2S_4$ nanosheets at ambient environment. Moreover, since the polymer is quite sensitive to the temperature (glass-transition temperature, T_g, $\approx$ 50 °C, Figure S5, SI), such an ambient reaction can make sure the 3D-printed OTL substrate possesses a high mechanical performance after coating nickel or generating $CoNi_2S_4$ nanosheets.

Figure 6

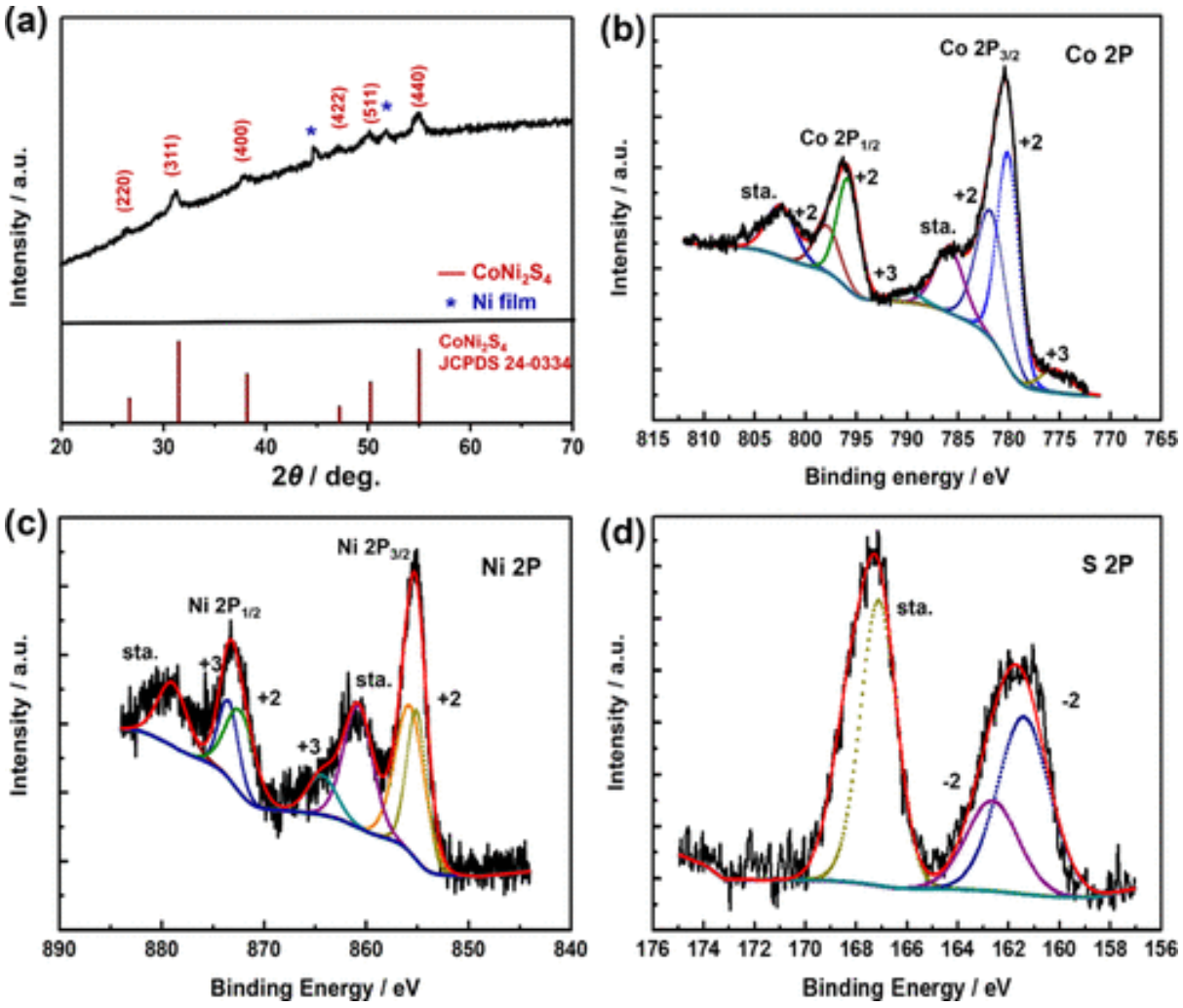

Figure 6. (a) XRD patterns of $CoNi_2S_4$ nanosheet with a spot of nickel films shafted from the $CoNi_2S_4$/Ni/OTL electrodes. XPS spectra of (b–d) Co 2p, Ni 2p, and S 2p for $CoNi_2S_4$ powders.

Figure 6b–d demonstrates the analysis results for chemical states in terms of different elements in $CoNi_2S_4$ assisted by X-ray photoelectron spectroscopy (XPS), in which the $CoNi_2S_4$ nanosheets were carefully peeled off from the as-obtained $CoNi_2S_4$/Ni/OTL electrodes. Both Ni and Co 2p spectra are approximately obtained via using two shakeup satellites (Sat.) and two spin–orbit doublets on the basis of Gaussian fitting function; see Figure 6b,c. For Co 2p spectrum (Figure 6b), the binding energies of the Co 2p peaks at ~794.13 and 777.62 eV can be ascribed to Co^{3+} and the ones at around 798.42 and 783.25 eV correspond to Co^{2+}. Furthermore, the intensity of Co^{2+} peaks is much higher than that of Co^{3+} peaks, suggesting most of Co element is Co^{2+} cations in the last substance. This result is also consistent with the chemical state of Co element in $CoNi_2S_4$. In the case of Ni 2p spectrum

(Figure 6c), the spectra of Ni $2p_{1/2}$ and Ni $2p_{3/2}$ are well consistent with the spin–orbit doublet characteristics of Ni^{3+} and Ni^{2+}. More specifically, the peaks at about 873.50 and 855.88 eV indicate Ni^{2+} cations, and the ones at ~875.18 and 857.40 eV represent Ni^{2+} cations. These results confirm the element states in the as-fabricated Co–Ni sulfide nanosheets coexist with the cations of Co^{2+}, Co^{3+}, Ni^{3+}, and Ni^{2+}, which has a positive influence on enhancing the electrochemical capacity of electrodes. In the S 2p spectrum (Figure 6d), the main peaks centered at around 162.0 and 163.2 eV are attributed to S $2p_{1/2}$ and S $2p_{3/2}$. To be more specific, the peak at about 163.2 eV attributes to the sulfur–metal bonds (Co–S and Ni–S bonds) whereas the one at about 162.0 eV is induced by the S^{2-} bonds.

In brief, by the TEM, XRD, and XPS analyses, the as-fabricated nickel film and Co–Ni sulfide nanosheets are Ni–P alloy and $CoNi_2S_4$, respectively.

2.2. Electrochemical Performances of $CoNi_2S_4$/Ni/OTL Electrode

The electrochemical behaviors of the $CoNi_2S_4$/Ni/OTL and Ni/OTL electrodes were explored via using a three-electrode system in 6 M KOH electrolyte, where the potentiostatic deposition times for $CoNi_2S_4$ nanosheets were controlled within 10, 15, and 20 min (defined as $CoNi_2S_4$-10, $CoNi_2S_4$-15, and $CoNi_2S_4$-20), respectively. Figure 7a illustrates the typical cyclic voltammetry (CV) behavior of $CoNi_2S_4$/Ni/OTL-15 with the potential window from 0 to 0.85 V. During the electrochemical sweeps, a pair of redox peaks was found in CV curves, giving an indication of obvious pseudocapacitive properties of the $CoNi_2S_4$ nanosheets and Ni film. Such redox peaks attribute to the redox behaviors of Co^{2+}/Co^{3+} and Ni^{2+}/Ni^{3+} transitions on the basis of the following reactions (41)

$$CoNi_2S_4 + 2OH^{-1} \leftrightarrow CoS_{2x}OH + 2NiS_{2-x}OH + 2e^- \quad \textbf{(1)}$$

$$CoS_{2x}OH + OH^- \leftrightarrow CoS_{2x}O + H_2O + e^- \quad \textbf{(2)}$$

When the sweep rate increases, the anodic peak rises and simultaneously cathodic peak declines, indicating rapid redox reactions between the electrodes and electrolyte and low electrochemical resistance within the electrodes. (42)Figure 7b demonstrates the galvanostatic charge–discharge (GCD) curves of $CoNi_2S_4$/Ni/OTL-15 electrode with a 0–0.6 V potential window. Approximately symmetric GCD curves are observed, which indicates a high

coulombic efficiency. Likewise, the obvious plateau further suggests the pseudocapacitive characteristic, corresponding to the redox peaks of the CV curves (Figure 7a). Figure 7c displays the CV curves of the $CoNi_2S_4$/Ni/OTL-10, -15, -20 electrodes and Ni/OTL electrode at a constant scan rate of 30 mV s^{-1}. Remarkably, all CV integrated areas for the $CoNi_2S_4$/Ni/OTL electrodes are much larger than those for the Ni/OTL electrode, signifying the outstanding pseudocapacitive characteristic of $CoNi_2S_4$ nanosheets, which benefits from these compelling structural/compositional advantages (Figure 4l). The GCD curves at 10 mA cm^{-3} further illustrate the discharge times for all the $CoNi_2S_4$/Ni/OTL electrodes are obviously higher than those for Ni/OTL electrode. Moreover, increasing the electrodeposition time can facilitate the growth of $CoNi_2S_4$ on the electrode, thereby resulting in obtaining a larger discharge time of $CoNi_2S_4$-15 compared to that of $CoNi_2S_4$-10. Yet, further increasing the deposition time can lead to the shortening of discharge time, which could be attributed to the agglomeration of $CoNi_2S_4$ nanosheets. Such a phenomenon, related to generating "dead volumes" on the surface of electrode, can decay the charge–discharge behavior, which has been verified in the previous work. (1) Therefore, the optimal deposition time for $CoNi_2S_4$ nanosheets was quantitatively determined to be 15 min.

Figure 7

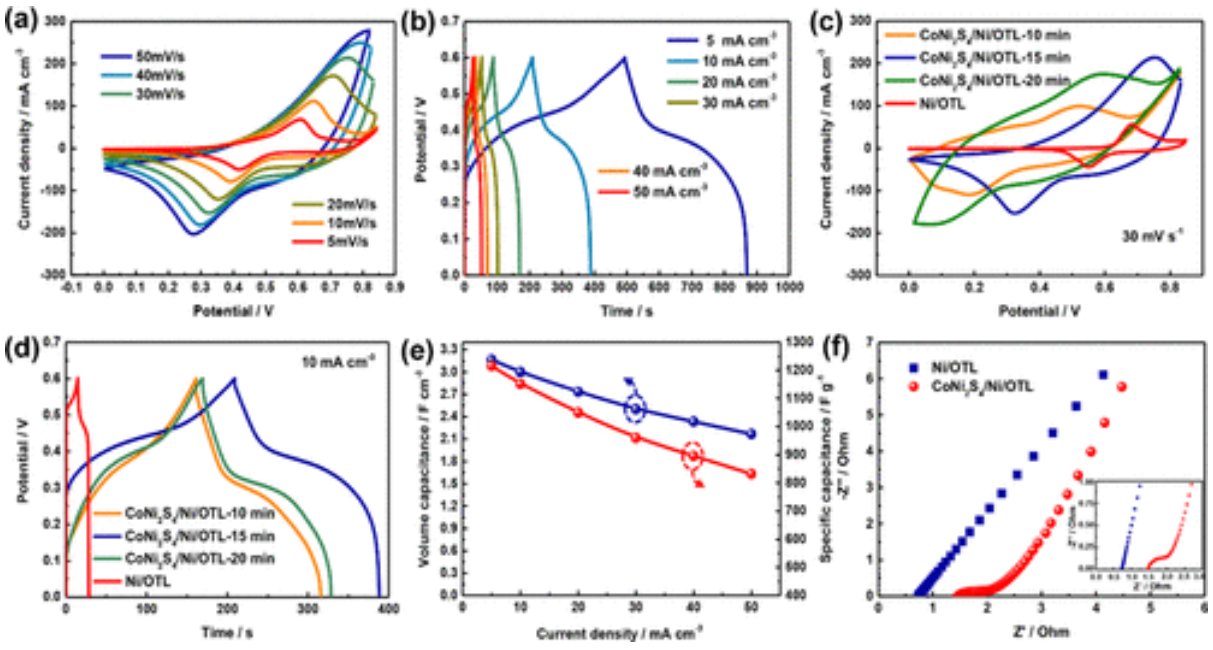

Figure 7. Electrochemical performances of the $CoNi_2S_4$/Ni/OTL electrodes measured by a three-electrode system: (a) CV curves of the $CoNi_2S_4$/Ni/OTL-15 electrode at different scanning speeds; (b) GCD curves of $CoNi_2S_4$/Ni/OTL-15 electrode at different current densities from 5 to 50 mA cm^{-3}; (c) CV curves of the $CoNi_2S_4$/Ni/OTL electrodes fabricated

with different times and Ni/OTL electrode; (d) GCD curves of the $CoNi_2S_4$/Ni/OTL electrodes fabricated with different times and Ni/OTL electrode; (e) volume and specific capacitances of $CoNi_2S_4$/Ni/OTL-15 electrode as a function of current density; (f) EIS curves of the $CoNi_2S_4$/Ni/OTL-15 and Ni/OTL electrodes. The inset is the magnification image of the corresponding EIS curves.

The volume/specific capacitance can be obtained from GCD curves of the electrode with $CoNi_2S_4$-15 nanosheets, and the related results are shown in Figure 7e. When the discharge current density rises, the volume (specific) capacitance gradually declines from 3.17 F cm^{-3} (1216 F g^{-1}) to 2.17 F cm^{-3} (832 F g^{-1}), indicating there is still a 69% initial capacitance even if the current density is magnified 10 times. Here, the values of specific capacitance at 5 mA cm^{-3} are comparable to other reported performances for oxide or metal sulfide electrodes, i.e., $CoNi_2S_4$/Ni foam (672 F g^{-1}, 1216 A g^{-1}), (43) $NiCo_2S_4$/Co_9S_8 (735 F g^{-1}, 5 A g^{-1}), (44) Co-S/Ni-S (1279 F g^{-1}, 5 A g^{-1}), (45) NiCo-LDH/rGO/Ni foam (900 F g^{-1}, 5 A g^{-1}), (46) and other materials' specific capacitances listed in Table S1, SI. Figure 7f illustrates the impedance spectra, where the slope for the $CoNi_2S_4$/Ni/OTL electrode is higher than that for the Ni/OTL electrode at the low-frequency domain, indicating a relatively low diffusion resistance contributes to the ion diffusion of electrolyte during the redox reaction.

2.3. Electrochemical Performances of the $CoNi_2S_4$/Ni/OTL//CM/Ni/OTL Asymmetric Supercapacitor

A lattice asymmetric all-solid-state supercapacitor (LASC) was assembled using $CoNi_2S_4$/Ni/OTL and CM/Ni/OTL electrodes as the anode and cathode, respectively (Figure 8a), where the electric resistance of $CoNi_2S_4$/Ni/OTL electrode is only ~9.3 Ω, which can be attributed to the uniform distribution nickel film (Figure 8b). The electrochemical performances of CM/Ni/OTL electrodes with various contents of carbon materials in a three-electrode system are demonstrated in Figures S7 and S8. Four proportions for carbon materials were fabricated, viz., 100% CNT (0% graphene), 80% CNT (20% graphene), 50% CNT (50% graphene), and 0% CNT (100% graphene). The corresponding CM/Ni/OTL electrodes were regarded as CM/Ni/OTL-100, CM/Ni/OTL-80, CM/Ni/OTL-50, and CM/Ni/OTL-0, respectively. The CV curves of CM/Ni/OTL electrodes at different scan speeds and contents are exhibited in Figure S7, in which all curves exhibit an electrical double-layer capacitance characteristic. Figure S8a–d exhibits approximately symmetric GCD curves, also indicating a good double-layer capacitance performance of CM/Ni/OTL electrodes. Moreover, when the

content of CNT is lower than 80%, the discharge time gradually prolongs with the increase of CNT, which can be ascribed to the carbon network architecture composed by CNT and graphene enhancing the electron/ion transport and thus improving the electrochemical performances of CM/Ni/OTL electrode. However, when the content of CNT reaches 100%, the corresponding performances significantly decrease, likely due to the formation of "dead volumes" or the stacking phenomenon of CNT. (1) The volume and specific capacitances with CM/Ni/OTL electrode can be obtained by eq 5, and the corresponding maximum values reach 597.6 mF cm^{-3} and 157.6 F g^{-1} at 1 mA cm^{-3} current density with a capacitance retention rate of 34.28% from 1 to 15 mA cm^{-3} (Figure S8e,f).

Figure 8

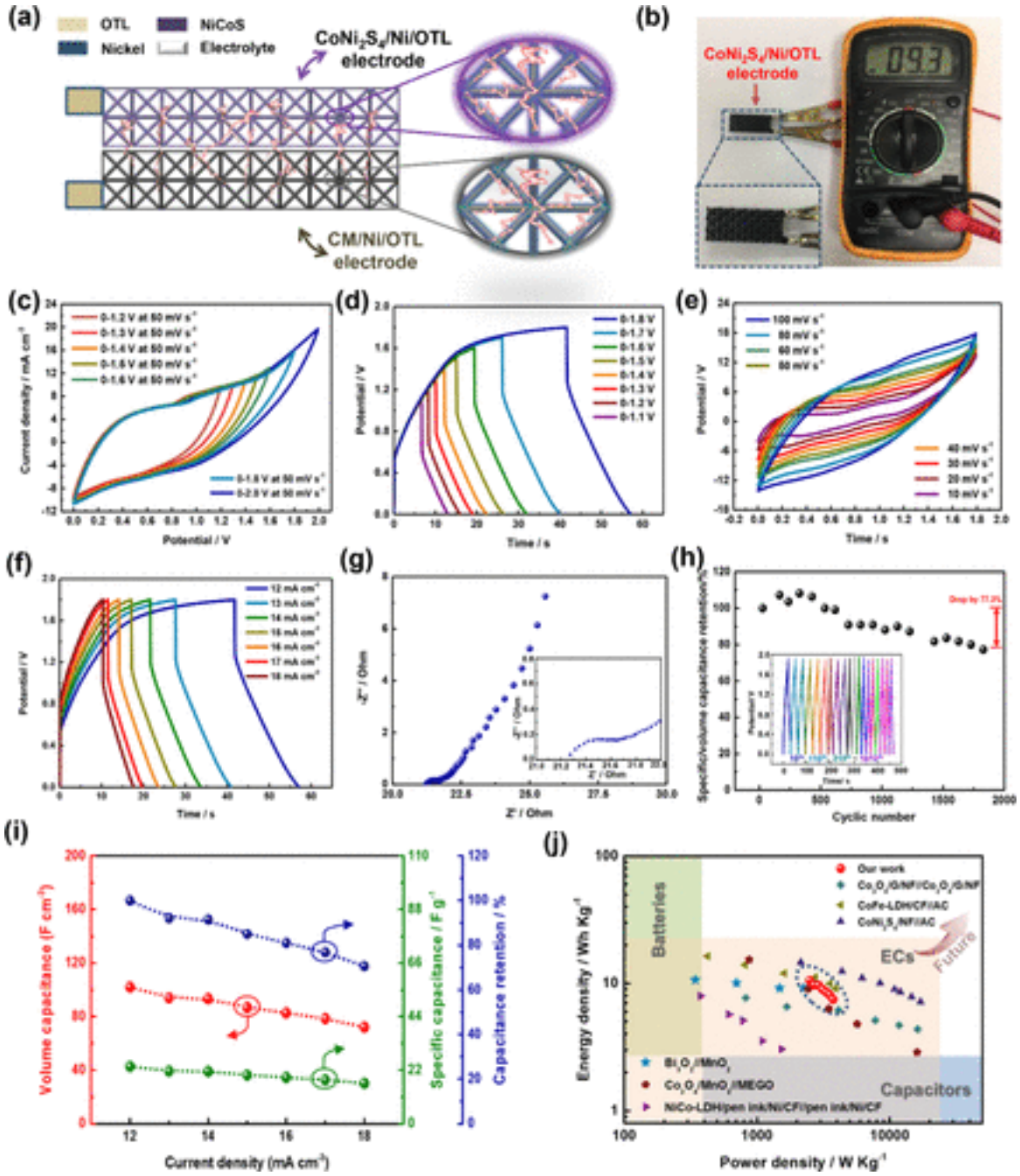

Figure 8. (a) Schematic diagram of the LASC based on 3D $CoNi_2S_4$/Ni/OTL and CM/Ni/OTL electrodes. (b) Schematic illustration of $CoNi_2S_4$/Ni/OTL electrode with the resistance of 9.3 Ω. (c) CV curves at different potential windows at a scan rate of 50 mV s^{-1}. (d) GCD curves at different potential windows at a constant current density of 6 mA cm^{-3}. (e) CV curves at various scan rates of 10–100 mV s^{-1}. (f) GCD curves at different current densities of 12–18 mA cm^{-3}. (g) EIS curves of the LASC. The inset is the magnification image of EIS curves of the LASC. (h) Cycling stability of the LASC. The inset shows the corresponding GCD curves at various

cyclic numbers. (i) Specific capacitance, volume capacitance, and capacitance retention of the LASC versus different current densities. (j) Ragone plot related to energy and power densities of the LASC and other supercapacitors.

To match the charge balance, we obtain $q^+ = q^-$, in which q^+ and q^- represent the whole charge of the anode and cathode.

$$q = C\Delta Vm$$

(3)

where C, ΔV, and m are the capacitance, potential window in GCD curve, and mass of activating materials.

Therefore, the mass ratio of activating materials in anode and cathode electrode theoretically is

$$\frac{m_+}{m_-} = \frac{C_-\Delta V_-}{C_+\Delta V_+}$$

(4)

wherein 0.14 can be obtained in this work.

Figure 8c displays CV curves of the LASC at a scan rate of 50 mV s^{-1}, suggesting the electrochemical potential window can be remarkably enlarged in comparison to that of individual electrode (Figure 7a). Furthermore, Figure 8d demonstrates GCD behaviors at various potential windows (0–1.8 V), demonstrating a stable charge–discharge behavior for supercapacitor upon to 1.8 V. Figure 8e shows the CV curves at various scan rates from 10 to 100 mV s^{-1}, in which two pairs of redox peaks are found, which are relevant with the redox reactions of $CoNi_2S_4$ nanosheets and nickel film. The configuration of CV curves for the LASC is similar to that for CM/Ni/OTL electrode at a low potential case, indicating that an electrical double-layer capacitance characteristic. Furthermore, all GCD curves (Figure 8f) confirm the charge–discharge capacity up to 1.8 V, giving an indication of possible application as a three-dimensional energy storage device (the GCD curves at the low current density of 2 mA cm^{-3} can be also shown in Figure S9, SI). But, there is a sharp drop segment at the initial discharge stage, suggesting the relatively large internal resistance within the LASC (Figure 8g). This phenomenon could be induced by the solicitation of PVA/KOH electrolyte and the relatively

larger network room in LASC (Figure 8a). The corresponding volume capacitance as well as capacitance retention are illustrated in Figure 8h, where the specific and volume capacitances are 23.5 F g^{-1} and 102 mF cm^{-3} at a discharge current of 12 mA cm^{-3}, respectively, and the specific capacitance still shows 70.6% capacitance retention even at the current density of 18 mA cm^{-3}. In addition, because the cyclic stability is an important item in practical application of the LASC, Figure 8i shows the specific capacitance retention still reaches 77.3% after 1800 cycles, demonstrating its superior stability.

The LASC illustrates a relatively high energy density of 10.6 Wh kg^{-1} at a power density of 2488.3 W kg^{-1}, in comparison with the electrochemical performance of existing supercapacitors together illustrated in Figure 8j (Co_3O_4/G/NF//Co_3O_4/G/NF, (47) CoFe-LDH/CF//AC, (48) $CoNi_2S_4$/NF//AC, (49) Bi_3O_2//MnO_3, (50) Co_3O_4/MnO_2//MEGO, (51) and NiCo-LDH/pen ink/Ni/CF//pen ink/Ni/CF, (37) where NF, G, LDH, CF, AC, MEGO represent nickel foam, graphene, layered double hydroxide, carbon fiber, activated carbon, and microwave exfoliated graphite oxide, respectively). Furthermore, even at a 3732.5 W kg^{-1} power density, it also possesses a 7.5 Wh kg^{-1} energy density, which is better than that reported for cobalt, nickel, and manganese-based pseudocapacitor supercapacitors.

Finally, we implemented two experiments to exhibit the practical energy storage capacity of as-fabricated LASCs; see Figures S10 and S11, SI.

3. Conclusions

In summary, we developed three-dimensional lattice asymmetric supercapacitors by 3D printing method for the first time. The 3D spatial framework and hierarchical feature of active materials on the surface of trusses can not only load more active materials but also benefit the electron/ion transport, thereby improving the energy density. In addition, the fabrication routes, including 3D printing, electroless plating, and electrodeposition technologies, were carried out at ambient temperature, which ensures the stability of a photopolymer substrate. Moreover, the configuration of printed octet-truss lattice structures and the amount of active materials can be fully controlled by 3D printing technology and electrochemical synthesis methods. The $CoNi_2S_4$/Ni/OTL electrodes display a high capacitance of 1216 F g^{-1} and good capacitance retention capability of 69% at 50 mA cm^{-3}. The resultant LASC with a 77.3% capacitance retention after 1800 cycles achieved a 10.6 Wh kg^{-1} energy density and 2488.3 W kg^{-1} power density. According to the above merits, we expect the design strategy can open a new route to

improve supercapacitors' energy density and the designed lattice electrodes/supercapacitors can become a new member in the family of electronic devices.

4. Experimental Section

4.1. Synthesis of Octet-Truss Lattice Substrate

Octet-truss lattice substrates were fabricated by using an industrial grade 3D photocurable printer (NOVA 3D) that is based on the typical stereolithography appearance (SLA) technology. Initially, a lattice substrate consisted of 5 × 10 × 1 sets of octet-truss unit cells with 4 mm unit size and a 0.5 mm strut diameter was designed by using CAD software (Siemens NX 10.0) and saved in stereolithography (STL) format. Subsequently, the file was imported into a preprocessing software (NOVA 3D-L101A) and the model was sliced with a slice height of 0.1 mm. Such a sliced model is used to control the photoroute to solidify the liquid photopolymer in a tank. After solidifying one layer from the bottom of the tank, an elevator lift with the printed object will rise. The process is continuously repeated until the 3D object is entirely printed. In accordance with this mechanism, the octa-truss lattice with a well-ordered internal configuration and fairly uniform surface morphology was successfully manufactured; see Figure 1.

4.2. Synthesis of Nickel/OTL Electrode

The nickel-coated lattice electrode was fabricated using the electroless plating technology. (52) Briefly, the as-prepared OTL substrate was first cleaned with deionized (DI) water. Subsequently, it was sensitized by 10 g L^{-1} $SnCl_2$ and activated with 0.5 g L^{-1} $PdCl_2$ for 15 min, respectively. After being dried at 80 °C, the electroless plating process was carried out; viz., the seeded OTL substrate was immersed in a 40 g L^{-1} $NiSO_4 \cdot 5H_2O$ solution at 90 °C for 5 min. Afterward, the nickel coated on OTL electrode was rinsed with DI water and dried at ambient temperature.

4.3. Synthesis of $CoNi_2S_4$/Ni/OTL Electrode

The solution was synthesized by completely mixing 10 mM $NiCl_2 \cdot 6H_2O$, 20 mM $CoCl_2 \cdot 6H_2O$, and 0.4 M thiourea in 50 mL of DI water. Afterward, the $CoNi_2S_4$/Ni/OTL electrode was fabricated on the basis of the three-electrode system. The electrodeposition potential was −1.0 V for 10, 20, and 30 min. The as-synthesized $CoNi_2S_4$/Ni/OTL was subsequently rinsed with DI water and dried at ambient temperature.

4.4. Synthesis of CM/Ni/OTL Electrode

Aqueous GO dispersion (~0.5 mg mL^{-1}) was first synthesized from graphite (Bay Carbon) following a modified Hummers method. (53) A mixture of MWCNT with graphene was applied as the active material of cathode electrode. The mass ratio of CNTs: graphene was fixed at 1, 0.8, 0.5 and 0, respectively. Then, the active material was blended with carboxyl methyl cellulose and acetylene black in a weight ratio of 75:10:15 with 40 mL of DI water as a dispersant. Subsequently, the resultant was laid in an ultrasonic bath for 10 h to obtain a homogeneous slurry.

The CM/Ni/OTL electrode was fabricated via using the dip-coating method. (1,37) The as-fabricated Ni/OTL electrode was immersed into the synthesized slurry for 5 min. It was carefully removed from the slurry and put on a vacuum oven at 80 °C for 20 min. By repeating the procedure, the expected mass of CM on Ni/OTL electrodes can be satisfied.

4.5. Microstructural and Element Characterizations

The morphologies of the activating materials were estimated by scanning electron microscopy (Tescan, VEGA3), transmission electron microscope (JEOL JEM 2100) equipped with energy dispersive X-ray spectroscopy, X-ray diffractometer (Rigaku SmartLab), X-ray photoelectron spectroscopy (ESCALAB 250), and dynamic mechanical analysis (DMA, Mettler Toledo). Moreover, the finite element analysis was carried out on ANSYS software.

4.6. Electrochemical Measurements

The electrochemical behaviors were conducted by an electrochemical workstation (Versa STAT3). The volume capacitance (C_V, F g^{-1}) and specific capacitance (C_m, F cm^{-3}) can be obtained by using eq 5 in GCD curves.

$$C_V = \frac{I\Delta t}{V_{ol}\Delta V}, \quad C_m = \frac{I\Delta t}{m\Delta V} \tag{5}$$

in which I, Δt, V_{ol}, m, and ΔV present the discharge current, discharge time, nominal volume of electrode, the mass of active material, and potential window.

Additionally, the energy density (Wh kg^{-1})and power density (w kg^{-1}) are obtained by:

$$E = \int UI \, dt = I \int U \, dt$$

$$P = 3600E/t$$

(6)

where U and I represent the potential window and discharge current of the supercapacitor, respectively. t is the corresponding discharge time.

Notes

The authors declare no competing financial interest.

Acknowledgments

The work has been partially supported by Research Grants Council, Hong Kong (grant no.152009/17E) and Hong Kong Polytechnic University (grant no. BBA3).

References

1. Gao, L.; Cao, K.; Zhang, H.; Li, P.; Song, J.; Surjadi, J. U.; Li, Y.; Sun, D.; Lu, Y. Rationally Designed Nickel Oxide Ravines@ Iron Cobalt-Hydroxides with Largely Enhanced Capacitive Performance for Asymmetric Supercapacitor. J. Mater. Chem. A 2017, 5, 16944– 16952, DOI: 10.1039/C7TA04998F
2. Kyerematenga, N. A.; Brousse, T.; Pech, D. Microsupercapacitors as Miniaturized Energy-Storage Components for on-Chip Electronics. Nat. Nanotechnol. 2017, 12, 7– 15, DOI: 10.1038/nnano.2016.196
3. Wang, G.; Zhang, L.; Zhang, J. A review of Electrode Materials for Electrochemical Supercapacitors. Chem. Soc. Rev. 2012, 41, 797– 828, DOI: 10.1039/C1CS15060J
4. Simon, P.; Gogotsi, Y. Materials for Electrochemical Capacitors. Nat. Mater. 2008, 7, 845– 854, DOI: 10.1038/nmat2297
5. Miller, J. R.; Simon, P. Electrochemical Capacitors for Energy Management. Sci. Mag. 2008, 321, 651– 652, DOI: 10.1126/science.1158736
6. Zhu, Y.; Murali, S.; Stoller, M. D.; Ganesh, K.; Cai, W.; Ferreira, P. J.; Pirkle, A.; Wallace, R. M.; Cychosz, K. A.; Thommes, M.Carbon-Based Supercapacitors Produced by Activation of Graphene. Science 2011, 332, 1537– 1541, DOI: 10.1126/science.1200770
7. Xue, Y.; Ding, Y.; Niu, J.; Xia, Z.; Roy, A.; Chen, H.; Qu, J.; Wang, Z. L.; Dai, L. Rationally Designed Graphene-Nanotube 3D Architectures with A Seamless Nodal Junction for Efficient Energy Conversion and Storage. Sci. Adv. 2015, 1, e1400198 DOI: 10.1126/sciadv.1400198
8. Sun, H.; Mei, L.; Liang, J.; Zhao, Z.; Lee, C.; Fei, H.; Ding, M.; Lau, J.; Li, M.; Wang, C.Three-Dimensional Holey-Graphene/Niobia Composite Architectures for Ultrahigh-Rate Energy Storage. Science 2017, 356, 599– 604, DOI: 10.1126/science.aam5852
9. Dai, S.; Guo, H.; Wang, M.; Liu, J.; Wang, G.; Hu, C.; Xi, Y. A Flexible Micro-Supercapacitor Based on A Pen Ink-Carbon Fiber Thread. J. Mater. Chem. A 2014, 2, 19665– 19669, DOI: 10.1039/C4TA03442B
10. Pu, X.; Li, L.; Liu, M.; Jiang, C.; Du, C.; Zhao, Z.; Hu, W.; Wang, Z. L. Wearable Self-Charging Power Textile Based on Flexible Yarn Supercapacitors and Fabric Nanogenerators. Adv. Mater. 2016, 28, 98– 105, DOI: 10.1002/adma.201504403

11. Pu, X.; Liu, M.; Li, L.; Han, S.; Li, X.; Jiang, C.; Du, C.; Luo, J.; Hu, W.; Wang, Z. L. Wearable Textile-Based in-Plane Microsupercapacitors. Adv. Energy Mater. 2016, 6, 1601254 DOI: 10.1002/aenm.201601254
12. Niu, Z.; Zhou, W.; Chen, X.; Chen, J.; Xie, S. Highly Compressible and All-Solid-State Supercapacitors Based on Nanostructured Composite Sponge. Adv. Mater. 2015, 27, 6002– 6008, DOI: 10.1002/adma.201502263
13. Tong, H.; Yue, S.; Jin, F.; Lu, L.; Meng, Q.; Zhang, X. Honeycomb-Like NiCo2O4@ Ni (OH)2 Supported on 3D N– Doped Graphene/Carbon Nanotubes Sponge as A High Performance Electrode for Supercapacitor. Ceram. Int. 2018, 44, 3113– 3121, DOI: 10.1016/j.ceramint.2017.11.078
14. Jiang, Q.; Li, G.; Wang, F.; Gao, X. Highly Ordered Mesoporous Carbon Arrays from Natural Wood Materials as Counter Electrode for Dye-Sensitized Solar Cells. Electrochem. Commun. 2010, 12, 924– 927, DOI: 10.1016/j.elecom.2010.04.022
15. Fleck, N.; Deshpande, V.; Ashby, M. In Micro-Architectured Materials: Past Present and Future. Proc. R. Soc. London, Ser. A 2010, 466, 2495– 2516, DOI: 10.1098/rspa.2010.0215
16. Dong, L.; Deshpande, V.; Wadley, H. Mechanical Response of Ti–6Al–4V Octet-Truss Lattice Structures. Int. J. Solids Struct. 2015, 60–61, 107– 124, DOI: 10.1016/j.ijsolstr.2015.02.020
17. Li, W.; Mak, C.; Kan, C.; Hui, C. Enhancing the Capacitive Performance of A Textile-Based CNT Supercapacitor. RSC Adv. 2014, 4, 64890– 64900, DOI: 10.1039/C4RA10450A
18. Cong, H.-P.; Ren, X.-C.; Wang, P.; Yu, S.-H. Energ. Environ. Flexible Graphene–Polyaniline Composite Paper for High-Performance Supercapacitor. Science 2013, 6, 1185– 1191, DOI: 10.1039/C2EE24203F
19. Gao, S.; Liao, F.; Ma, S.; Zhu, L.; Shao, M. Network-Like Mesoporous NiCo 2O4 Grown on Carbon Cloth for High-Performance Pseudocapacitors. J. Mater. Chem. A 2015, 3, 16520– 16527, DOI: 10.1039/C5TA02876K
20. Chen, L.; Zhou, Y.; Dai, H.; Yu, T.; Liu, J.; Zou, Z. One-Step Growth of CoNi2S4 Nanoribbons on Carbon Fibers as Platinum-Free Counter Electrodes for Fiber-Shaped Dye-Sensitized Solar Cells with High Performance: Polymorph-Dependent Conversion Efficiency. Nano Energy 2015, 11, 697– 703, DOI: 10.1016/j.nanoen.2014.11.047

21. Ye, A.; Sui, Y.; Han, Y.; Sun, Z.; Qi, J.; Wei, F.; He, Y.; Meng, Q. Novel Corn Cob-Like Fe3O4@ Ni3S2 as High-Performance Electrode for Supercapacitors. Funct. Mater. Lett. 2017, 10, 1750062 DOI: 10.1142/S179360471750062X
22. Mohammadi, A.; Arsalani, N.; Tabrizi, A. G.; Moosavifard, S. E.; Naqshbandi, Z.; Ghadimi, L. S. Engineering rGO-CNT Wrapped Co3S4 Nanocomposites for High-Performance Asymmetric Supercapacitors. Chem. Eng. J. 2018, 334, 66– 80, DOI: 10.1016/j.cej.2017.10.029
23. He, W.; Wang, C.; Li, H.; Deng, X.; Xu, X.; Zhai, T. Ultrathin and Porous Ni3S2/CoNi2S4 3D-Network Structure for Superhigh Energy Density Asymmetric Supercapacitors. Adv. Energy Mater. 2017, 7, 1700983 DOI: 10.1002/aenm.201700983
24. Chen, Y.; Xu, B.; Wen, J.; Gong, J.; Hua, T.; Kan, C. W.; Deng, J. Design of Novel Wearable, Stretchable, and Waterproof Cable-Type Supercapacitors Based on High-Performance Nickel Cobalt Sulfide-Coated Etching-Annealed Yarn Electrodes. Small 2018, 14, 1704373 DOI: 10.1002/smll.201704373
25. Zhou, S.; Chen, J.; Gan, L.; Zhang, Q.; Zheng, Z.; Li, H.; Zhai, T. Scalable Production of Self-Supported WS2/CNFs by Electrospinning as the Anode for High-Performance Lithium-Ion Batteries. Sci. Bull. 2016, 61, 227– 235, DOI: 10.1007/s11434-015-0992-8
26. Xia, X.; Zhu, C.; Luo, J.; Zeng, Z.; Guan, C.; Ng, C. F.; Zhang, H.; Fan, H. J. Synthesis of Free-Standing Metal Sulfide Nanoarrays via Anion Exchange Reaction and Their Electrochemical Energy Storage Application. Small 2014, 10, 766– 773, DOI: 10.1002/smll.201302224
27. Yang, J.; Yu, C.; Fan, X.; Liang, S.; Li, S.; Huang, H.; Ling, Z.; Hao, C.; Qiu, J. Electroactive Edge site-Enriched Nickel–Cobalt Sulfide into Graphene Frameworks for High-Performance Asymmetric Supercapacitors. Energy Environ. Sci. 2016, 9, 1299– 1307, DOI: 10.1039/C5EE03633J
28. Yu, X. Y.; Yu, L.; Shen, L.; Song, X.; Chen, H.; Lou, X. W. D. General Formation of MS (M = Ni, Cu, Mn) Box-in-Box Hollow Structures with Enhanced Pseudocapacitive Properties. Adv. Funct. Mater. 2014, 24, 7440– 7446, DOI: 10.1002/adfm.201402560
29. Zheng, X.; Lee, H.; Weisgraber, T. H.; Shusteff, M.; DeOtte, J.; Duoss, E. B.; Kuntz, J. D.; Biener, M. M.; Ge, Q.; Jackson, J. A.Ultralight, Ultrastiff Mechanical Metamaterials. Science 2014, 344, 1373– 1377, DOI: 10.1126/science.1252291

30. Bauer, J.; Hengsbach, S.; Tesari, I.; Schwaiger, R.; Kraft, O. High-Strength Cellular Ceramic Composites with 3D Microarchitecture. Proc. Natl. Acad. Sci. USA 2014, 111, 2453– 2458, DOI: 10.1073/pnas.1315147111
31. Gu, X. W.; Greer, J. R. Ultra-Strong Architected Cu Meso-Lattices. Extreme Mech. Lett. 2015, 2, 7– 14, DOI: 10.1016/j.eml.2015.01.006
32. Schaedler, T. A.; Jacobsen, A. J.; Torrents, A.; Sorensen, A. E.; Lian, J.; Greer, J. R.; Valdevit, L.; Carter, W. B. Ultralight Metallic Microlattices. Science 2011, 334, 962– 965, DOI: 10.1126/science.1211649
33. Gao, F.; Xu, B.; Wang, Q.; Cai, F.; He, S.; Zhang, M.; Wang, Q. Potentiostatic Deposition of CoNi2S4 Nanosheet Arrays on Nickel Foam: Effect of Deposition Time on the Morphology and Pseudocapacitive Performance. J. Mater. Sci. 2016, 51, 10641– 10651, DOI: 10.1007/s10853-016-0286-9
34. Mohsenizadeh, M.; Gasbarri, F.; Munther, M.; Beheshti, A.; Davami, K. Additively-Manufactured Lightweight Metamaterials for Energy Absorption. Mater. Des. 2018, 139, 521– 530, DOI: 10.1016/j.matdes.2017.11.037
35. Gao, L.; Song, J.; Jiao, Z.; Liao, W.; Luan, J.; Surjadi, J. U.; Li, J.; Zhang, H.; Sun, D.; Liu, C. T. High-Entropy Alloy (HEA)-Coated Nanolattice Structures and Their Mechanical Properties. Adv. Eng. Mater. 2017, 20, 1700625 DOI: 10.1002/adem.201700625
36. Hu, W.; Chen, R.; Xie, W.; Zou, L.; Qin, N.; Bao, D. CoNi2S4 Nanosheet Arrays Supported on Nickel Foams with Ultrahigh Capacitance for Aqueous Asymmetric Supercapacitor Applications. ACS Appl. Mater. Interfaces 2014, 6, 19318– 19326, DOI: 10.1021/am5053784
37. Gao, L.; Utama, S. J.; Cao, K.; Zhang, H.; Li, P.; Xu, S.; Jiang, C.; Song, J.; Sun, D.; Lu, Y. Flexible Fiber-Shaped Supercapacitor Based on Nickel-Cobalt Double Hydroxide and Pen Ink Electrodes on Metallized Carbon Fiber. ACS Appl. Mater. Interfaces 2017, 9, 5409– 5418, DOI: 10.1021/acsami.6b16101
38. Lian, J.; Jang, D.; Valdevit, L.; Schaedler, T. A.; Jacobsen, A. J.; B. Carter, W.; Greer, J. R. Catastrophic vs Gradual Collapse of Thin-Walled Nanocrystalline Ni Hollow Cylinders as Building Blocks of Microlattice Structures. Nano Lett. 2011, 11, 4118– 4125, DOI: 10.1021/nl202475p

39. Shen, J.; Xu, X.; Dong, P.; Zhang, Z.; Baines, R.; Ji, J.; Pei, Y.; Ye, M. Design and Synthesis of Three-Dimensional Needle-Like CoNi2S4/CNT/Graphene Nanocomposite with Improved Electrochemical Properties. Ceram. Int. 2016, 42, 8120– 8127, DOI: 10.1016/j.ceramint.2016.02.016
40. Miao, P.; He, J.; Sang, Z.; Zhang, F.; Guo, J.; Su, D.; Yan, X.; Li, X.; Ji, H. Hydrothermal Growth of 3D Graphene on Nickel Foam as A Substrate of Nickel-Cobalt-Sulfur for High-Performance Supercapacitors. J. Alloy. Compd. 2018, 732, 613– 623, DOI: 10.1016/j.jallcom.2017.10.243
41. Mei, L.; Yang, T.; Xu, C.; Zhang, M.; Chen, L.; Li, Q.; Wang, T. Hierarchical Mushroom-Like CoNi2S4 Arrays as A Novel Electrode Material for Supercapacitors. Nano Energy 2014, 3, 36– 45, DOI: 10.1016/j.nanoen.2013.10.004
42. Yuan, C.; Li, J.; Hou, L.; Zhang, X.; Shen, L.; Lou, X. W. D. Ultrathin Mesoporous NiCo2O4 Nanosheets Supported on Ni Foam as Advanced Electrodes for Supercapacitors. Adv. Funct. Mater. 2012, 22, 4592– 4597, DOI: 10.1002/adfm.201200994
43. Pu, J.; Wang, T.; Wang, H.; Tong, Y.; Lu, C.; Kong, W.; Wang, Z. Direct Growth of NiCo2S4 Nanotube Arrays on Nickel Foam as High-Performance Binder-Free Electrodes for Supercapacitors. ChemPlusChem 2014, 79, 577– 583, DOI: 10.1002/cplu.201300431
44. Hou, L.; Shi, Y.; Zhu, S.; Rehan, M.; Pang, G.; Zhang, X.; Yuan, C. Hollow Mesoporous Hetero-NiCo2S4/Co9S8 Submicro-Spindles: Unusual Formation and Excellent Pseudocapacitance Towards Hybrid Supercapacitors. J. Mater. Chem. A 2017, 5, 133– 144, DOI: 10.1039/C6TA05788H
45. Li, X.; Li, Q.; Wu, Y.; Rui, M.; Zeng, H. Two-Dimensional, Porous Nickel–Cobalt Sulfide for High-Performance Asymmetric Supercapacitors. ACS Appl. Mater. Interfaces 2015, 7, 19316– 19323, DOI: 10.1021/acsami.5b05400
46. Bai, X.; Liu, Q.; Zhang, H.; Liu, J.; Li, Z.; Jing, X.; Yuan, Y.; Liu, L.; Wang, J. Nickel-Cobalt Layered Double Hydroxide Nanowires on Three Dimensional Graphene Nickel Foam for High Performance Asymmetric Supercapacitors. Electrochim. Acta 2016, 215, 492– 499, DOI: 10.1016/j.electacta.2016.08.134
47. Deng, X.; Li, J.; Zhu, S.; He, F.; He, C.; Liu, E.; Shi, C.; Li, Q.; Zhao, N. Metal–Organic Frameworks-Derived Honeycomb-Like Co3O4/Three-Dimensional Graphene Networks/Ni Foam Hybrid as A Binder-Free Electrode for Supercapacitors. J. Alloy. Compd. 2017, 693, 16– 24, DOI: 10.1016/j.jallcom.2016.09.096

48. Ma, K.; Cheng, J.; Liu, F.; Zhang, X. Co-Fe Layered Double Hydroxides Nanosheets Vertically Grown on Carbon Fiber Cloth for Electrochemical Capacitors. J. Alloy. Compd. 2016, 679, 277– 284, DOI: 10.1016/j.jallcom.2016.04.059
49. Zhu, Y.; Ji, X.; Wu, Z.; Liu, Y. NiCo2S4 Hollow Microsphere Decorated by Acetylene Black for High-Performance Asymmetric Supercapacitor. Electrochim. Acta 2015, 186, 562– 571, DOI: 10.1016/j.electacta.2015.10.176
50. Xu, H.; Hu, X.; Yang, H.; Sun, Y.; Hu, C.; Huang, Y. Flexible Asymmetric Micro-Supercapacitors Based on Bi2O3 and MnO2 Nanoflowers: Larger Areal Mass Promises Higher Energy Density. Adv. Energy Mater. 2015, 5, 1401882 DOI: 10.1002/aenm.201401882
51. Huang, M.; Zhang, Y.; Li, F.; Zhang, L.; Wen, Z.; Liu, Q. Facile Synthesis of Hierarchical Co3O4@ MnO2 Core–Shell Arrays on Ni Foam for Asymmetric Supercapacitors. J. Power Sources 2014, 252, 98– 106, DOI: 10.1016/j.jpowsour.2013.12.030
52. Gao, L.; Surjadi, J. U.; Cao, K.; Zhang, H.; Li, P.; Xu, S.; Jiang, C.; Song, J.; Sun, D.; Lu, Y. Flexible Fiber-Shaped Supercapacitor Based on Nickel–Cobalt Double Hydroxide and Pen Ink Electrodes on Metallized Carbon Fiber. ACS Appl. Mater. Interfaces 2017, 9, 5409– 5418, DOI: 10.1021/acsami.6b16101
53. Hummers, W. S., Jr.; Offeman, R. E. Preparation of Graphitic Oxide. J. Am. Chem. Soc. 1958, 80, 1339, DOI: 10.1021/ja01539a017

Supporting Information

Fully Controllable Design and Fabrication of Three-Dimensional Lattice Supercapacitors

Jian Song[a,b]*, *Yuejiao Chen*[b,d], *Ke Cao*[c], *Yang Lu*[c], *John H. Xin*[b], *Xiaoming Tao*[b]*

[a] College of Civil Engineering, Shenzhen University, Shenzhen, 518000, China

[b] Nanotechnology Center of Functional and Intelligent Textiles and Apparel, Institute of Textiles and Clothing, The Hong Kong Polytechnic University, Hong Kong, 999077, China.

[c] Department of Mechanical and Biomedical Engineering, City University of Hong Kong, 83 Tat Chee Avenue, Kowloon, Hong Kong, 999077,China.

[d] State Key Laboratory of Powder Metallurgy, Central South University, Changsha, 410083, China.

Corresponding Authors*E-mail: dfsongjian2006@126.com;

*E-mail: taoxiaoming@polyu.edu.hk

1. Finite element analysis for various lattice structures

1.1 Geometric and finite element models

To find out the most suitable lattice substrate, finite element analysis was performed by using ANSYS© software based on three different types of lattice structures, viz. Body-centered cubic-like (BCC-like) lattice, Face-centered cubic-like (FCC-like) lattice and Oct-truss lattice (OTL), respectively. Because an OTL structure can be divided into a BCC-like lattice structure and FCC lattice structure (**Figure S1c**), the geometric models of the lattice structure with 3×3×3 OTL units and the corresponding nickel coated OTL structure were displayed in **Figure S1a,b**. Here, each cubic OTL substrate includes 24 trusses with the diameter of 0.5 mm, and the side length is 4 mm, and there are 24 trusses with the diameter of 0.5 mm. The 8-node quadrilateral element (solid-185) was used to discrete the overall structure. The modulus of polymer is 2400 MPa obtained from the ABS-M30 standard (Advanced FDM Technology™),[1] while the modulus of nickel film is 3093 MPa obtained by Nanoindentation test (**Figure S3c,d**).

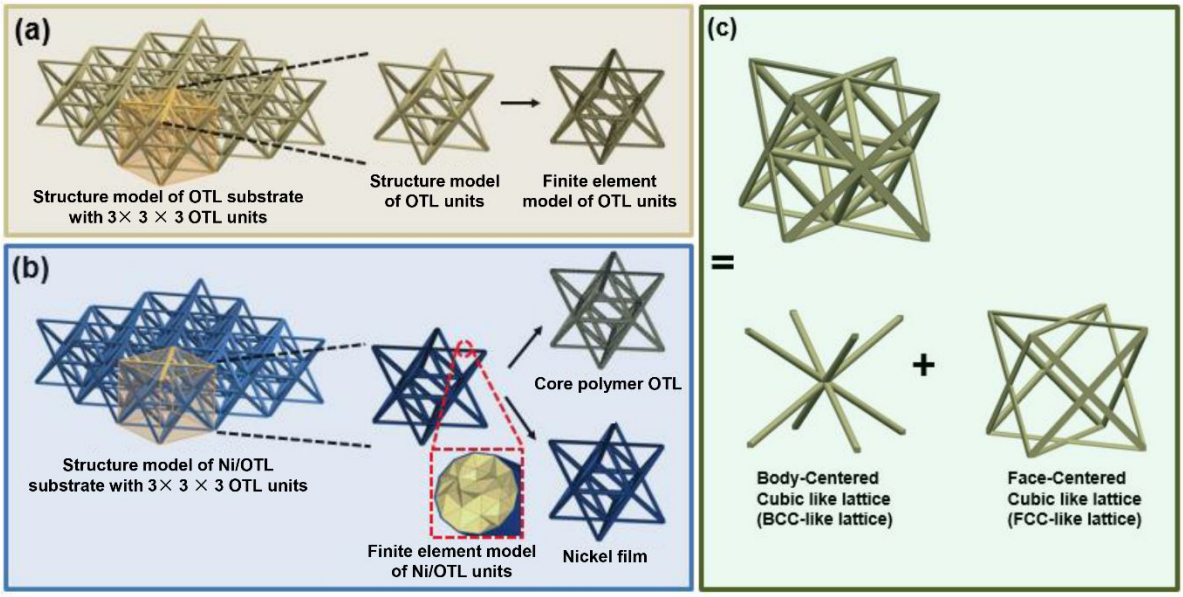

Figure S1. Geometric model and FEM model. (a) Oct-truss lattice substrate with 3×3×1 units. (b) Ni/OTL OTL lattice substrate with 3×3×1 units, here the nickel film with a one-layer structure uniformly distributes on the surface of OTL. (c) Decomposition structure of OTL.

1.2 Finite element analysis

After implementing the compression load of 1 N along the Z-axis direction, the equivalent stress responses with respect to different substrates were shown in **Figure S2**.

The bending-dominated and tension-dominated deformations were clearly observed in **Figure S2a,b**, respectively. However, for the OTL structure, when it is subjected to the compression loading, the external FCC-like component to some degree limits the free deformation of internal BCC-like lattice that can bear higher loading level, resulting in a remarkably decline of overall stress level in OTL

structure (**Figure S2c**). In addition, compared with the OTL substrate, the metal nickel film can efficiently decrease the stress level of core polymer in Ni/OTL substrate (**Figure S2c,d**), dropping by ~30%, and simultaneously make the structure conductivity. Therefore, the OTL framework was selected as the basic substrate of supercapacitor in this work.

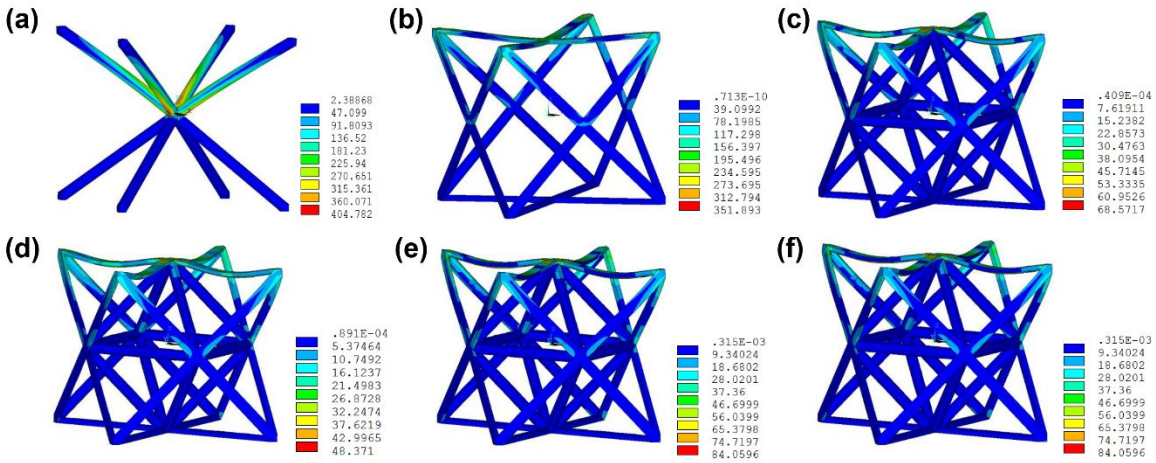

Figure S2. Equivalent stress contours of (a) BCC-like lattice, (b) FCC-like lattice, (c) OTL, (d) Core polymer in OTL, (e) Nickel film in OTL, (f) Ni/OTL composites.

2. Characterization of as-fabricated nickel film

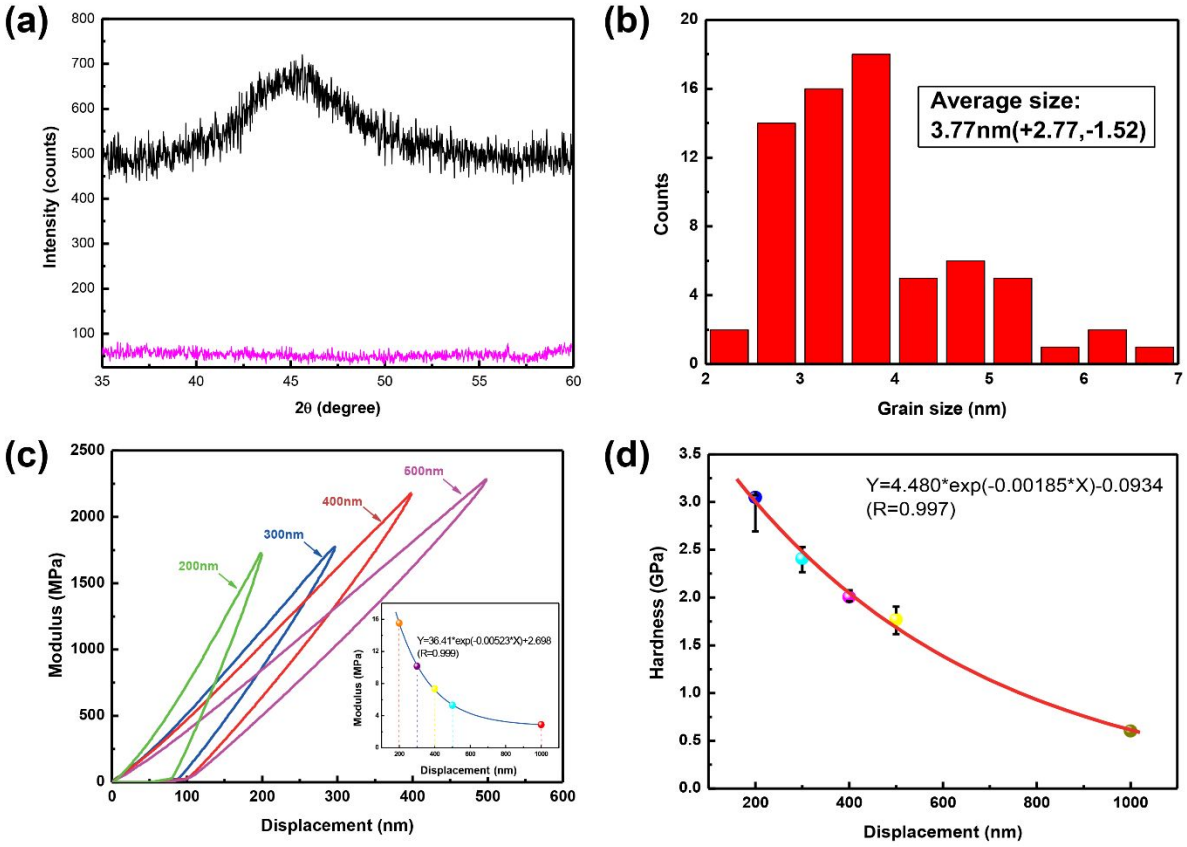

Figure S3. (a) XRD analysis for as-fabricated Ni-P metal. (b) Histogram of grain size. (c-d) Nanoindentation and hardness of Ni-P nanopillar under different depths, inset c is the relationship between the modulus and depth, inset d is the relationship between the hardness and depth.

3. TEM analysis of graphene and MWCNT

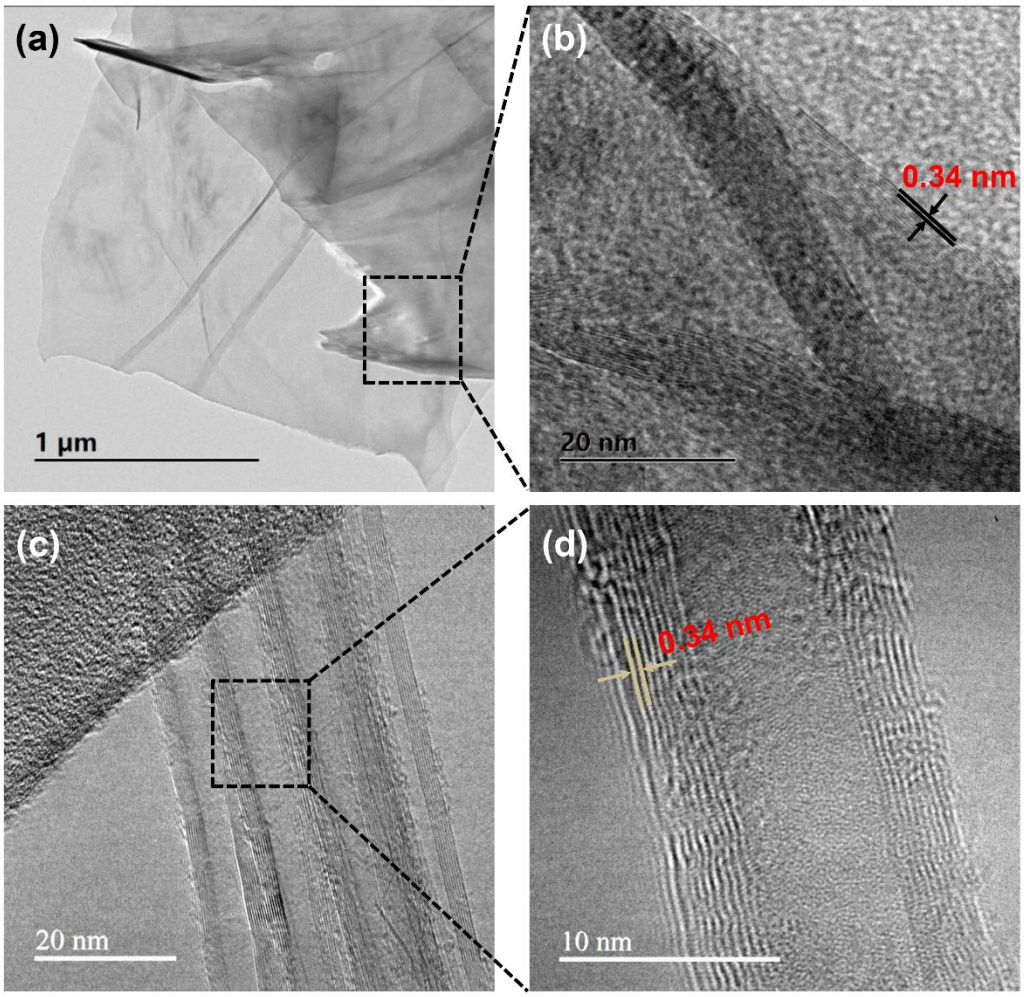

Figure S4. TEM analysis for graphene and MWCNT. (a-b) Graphene. (c-d) MWCNT

4. DMA analysis of photopolymer

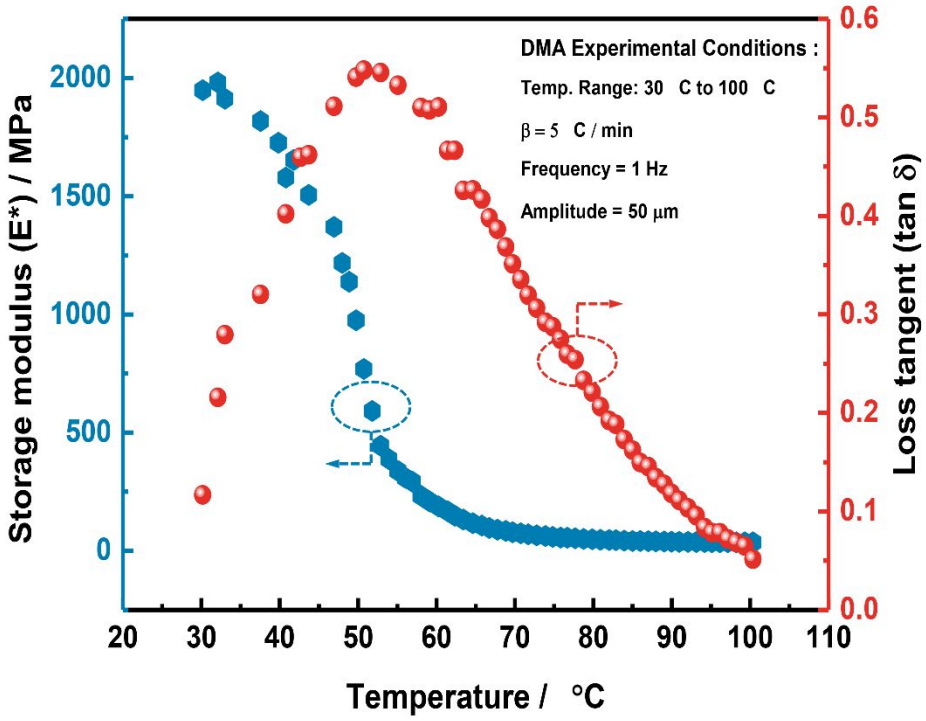

Figure S5. DMA curve of photopolymer.

5. BET surface area test

The Brunauer-Emmett-Teller (BET, NOV Atouch^{TM}) surface area was obtained from the Nitrogen adsorption/ desorption isotherm recorded at 77 K and the pore size distribution was calculated via using the Barrett-Joyner-Halenda (BJH) method. The $CoNi_2S_4$ nanosheets were firstly synthesized by using electrodeposition method (***Experimental Section***, ***Manuscript***) on a piece of smooth steel disc, and after drying, numbers of $CoNi_2S_4$ powders were easily shaved from it. Likewise, the nickel films were fabricated by using electroless plating method on the steel disc, following by a shaving operation to collect nickel films. Additionally, the carbon materials were fabricated by mixing by MWCNT, graphene and acetylene black (The mass ratio is 4:1:1), followed by a dip-coating method to obtain carbon material powders.

Figure S6 demonstrates the BET surface area and pore size distribution of as-fabricated $CoNi_2S_4$ powders, nickel films and carbon material powders. Figure S6(a-c) illustrates that there is a type-IV isotherm with a H3 hysteresis loop in each of nitrogen adsorption and desorption curves, indicating the presence of porous structure of as-fabricated activate materials. Furthermore, the pore size distribution curves inset in Figure S6(a-c) obviously exhibit predominant peaks for $CoNi_2S_4$ are approximately lower than 1 nm, whereas the ones for nickel and carbon materials are larger than 1 nm, which suggests that the $CoNi_2S_4$

nanosheets can provide more routes to transmit electrons/ ions between electrolyte and hierarchical activate materials in each area. Furthermore, both nickel films and solidified carbon materials have higher surface area, thereby resulting in loading more activate materials to form the hierarchical structure.

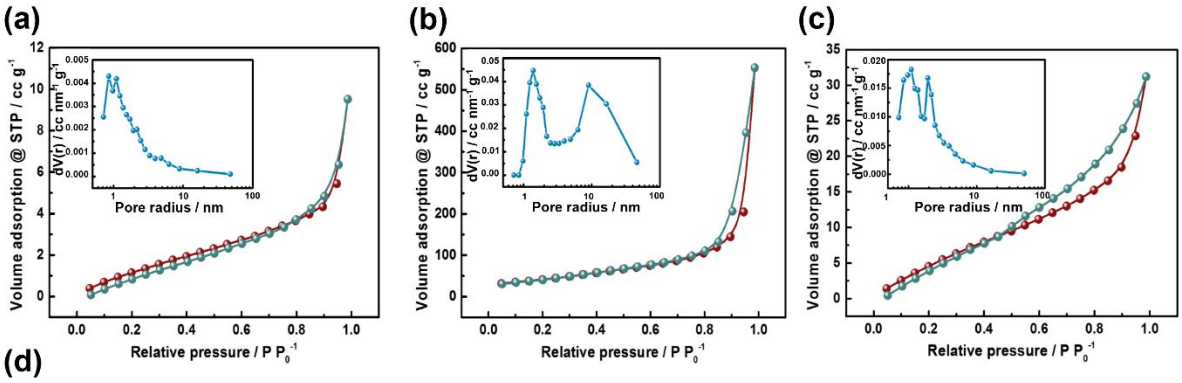

(d)

	Surface area / m^2 g^{-1}	Pore volume / cc g^{-1}	Pore radius / nm
$CoNi_2S_4$ powder	10.470	0.0176	0.850
Carbon materials	172.799	0.866	1.380
Nickel film	48.474	0.0616	1.101

Figure S6. BET data. (a) CoNi2S4 powders. (b) Carbon material powders. (c) Nickel films. (d) Test values of surface area, pore volume and pore radius. The insets in part (a)-(c) are the corresponding pore size distribution.

6. Electrochemical performance of CM/Ni/OTL

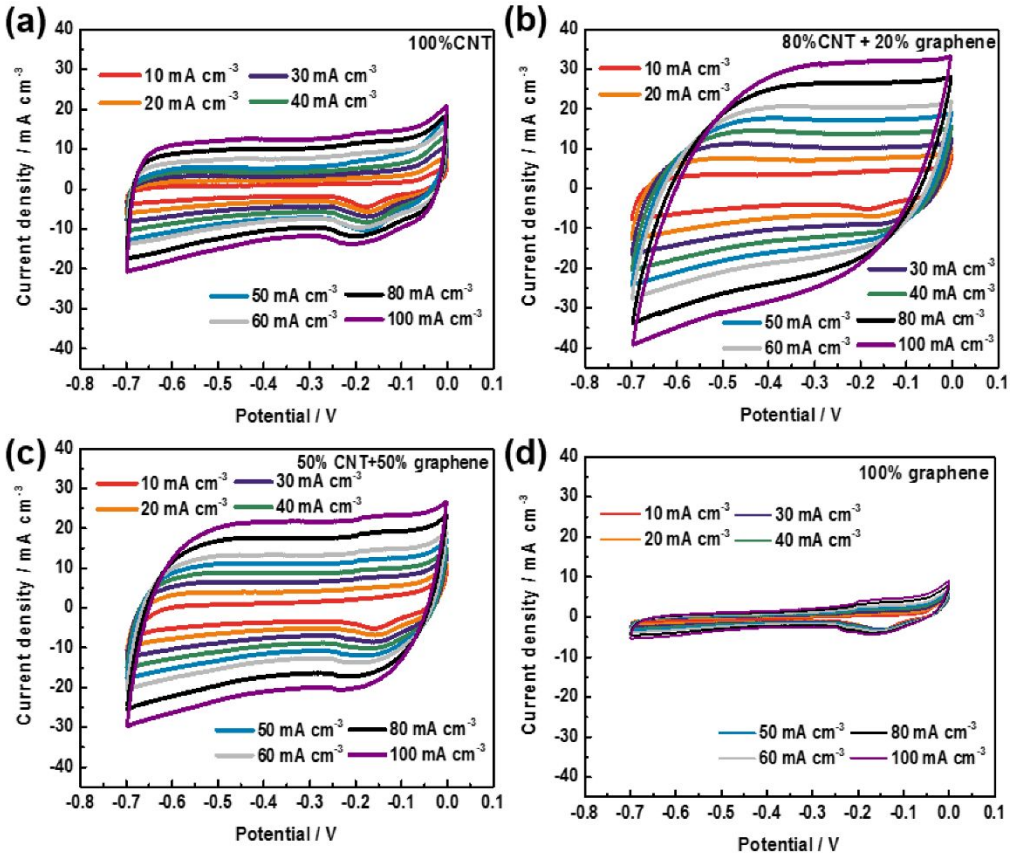

Figure S7. CV curves of CM/Ni/OTLs at different scan speeds and CNT contents. (a) 100% CNT. (b) 80% CNT and 20% graphene. (c) 50% CNT and 50% graphene. (d)100% graphene.

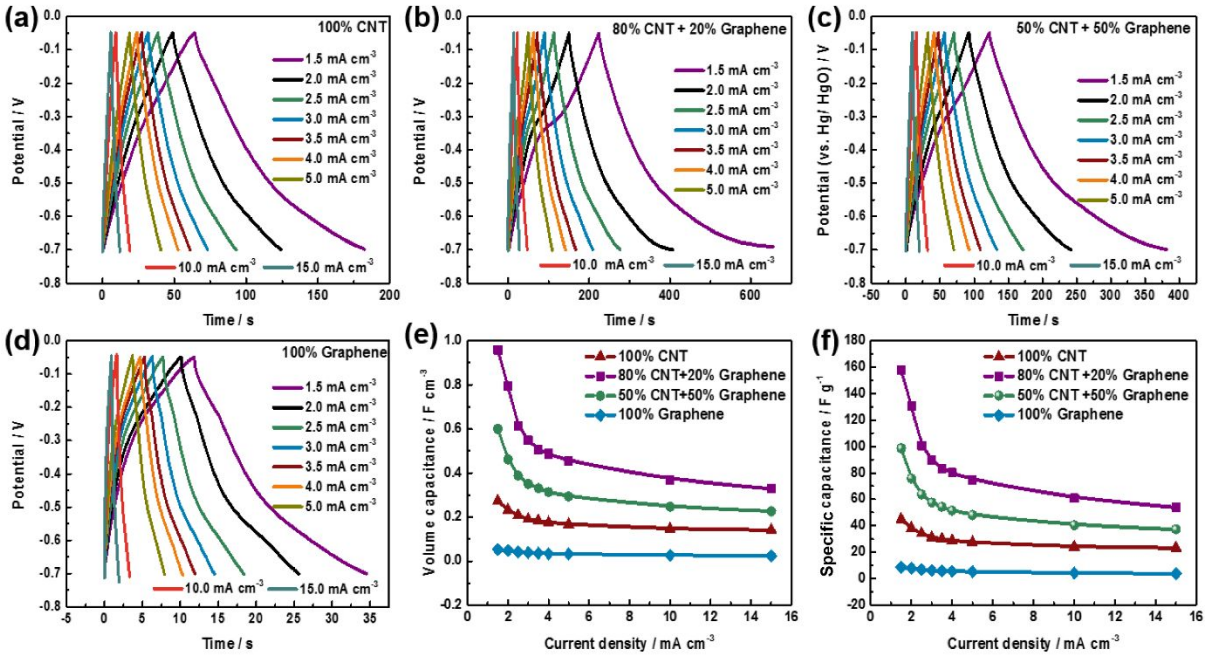

Figure S8. (a-d) GCD curves of CM/Ni/OTLs at different scan speeds and CNT contents. (e-f) Volume capacitance and specific capacitance of CM/Ni/OTL electrodes versus different current density.

7. GCD curves of the LASC at the low current density

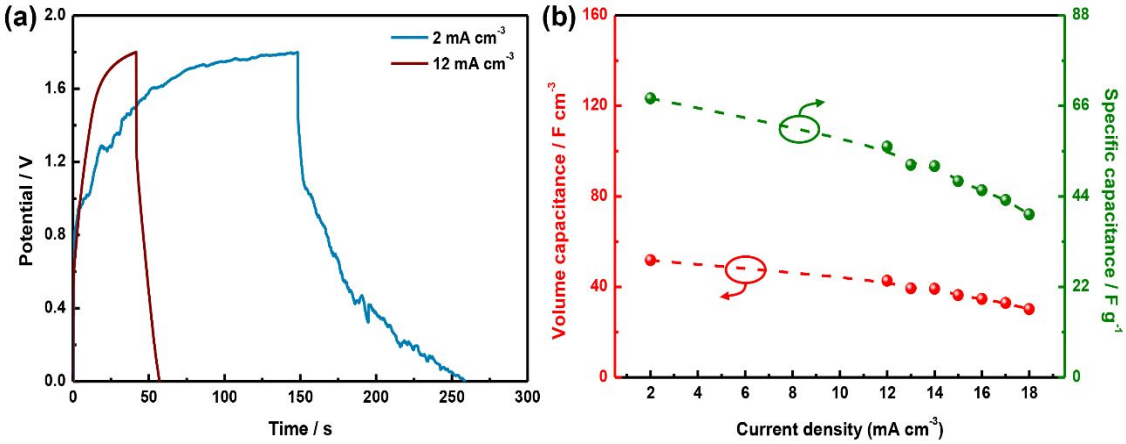

Figure S9 (a) GCD curves of the LASC at different current densities of 2 and 12 mA cm^{-3}. Here, the curve at the current density of 12 mA cm^{-3} has been shown in Figure 8f, in Manuscript. (b) Specific/ volume capacitances of LASC as a function of current density.

8. Fabrication of triboelectric nanogenerator

A large-area, ultraflexible and free-standing fiber-based triboelectric nanogenerator (FTNG) was fabricated, which would charge for as-fabricated supercapacitors. The contact-mode FTNG was made from a commercial Ag-coated chinlon fabric (Ag@CF) as electropositive material as well as conductive electrode and a polydimethylsiloxane (PDMS) coated Ag@CF (PDMS-based Ag@CF) composite layer as the electronegative material. **Figure S10a** exhibits the schematic image of the fabricated FTNG, which can be driven by a rigid four-springe auxiliary device. **Figure S10b** shows the photographs of FTNG devices. The scanning electron microscopy (SEM) diagram of PDMS-based Ag@CF was shown in **Figure S10c**, demonstrating that the Ag@CF is thoroughly coated by PDMS. **Figure S10d** illustrates that the fabrication process of PDMS-based Ag@CF composite layer. This layer was facile fabricated by a doctor-blading method. More specifically, the PDMS and cross-linking agent (XF15-645, Momentive) were homogeneously mixed with a mass ratio of 1:1 to fabricate PDMS solution. Afterwards, a substrate, via. sandpaper, was attached to a glass pane using double-sided tapes, following that the as-prepared PDMS solution was cast at the one side of substrate. A doctor-blading operation was performed to form a uniform PDMS film via pushing a glass rod carefully. Subsequently, a large-area Ag@CF was immediately covered on the

surface of PDMS layer. Finally, the PDMS-based Ag@ CF composite layer was cured at 80 ℃ for 3 hours and easily peeled off from the substrate owing to the sandpaper substrate. **Figure S10e** exhibits the large-area, ultraflexible and free-standing PDMS-based Ag@ CF composite layer.

The FTNG were compressed by Keyboard Life Tester (ZXA-03), and the output signal was collected by Keisight DSO-X3014A oscilloscope.

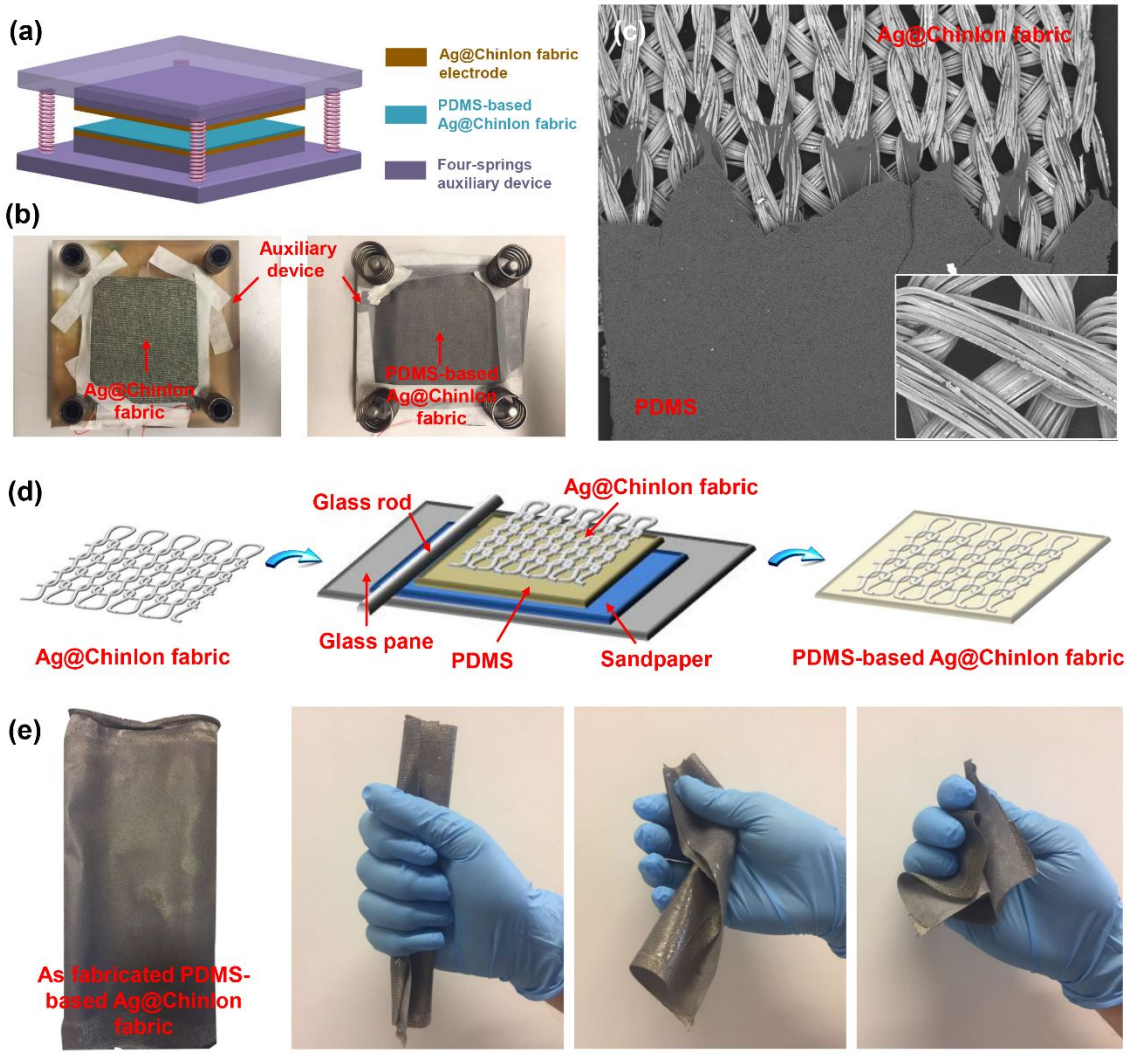

Figure S10. (a) Schematic image of FTNG. (b) Photograph of FTNG. (c) SEM

image of PDMS-based Ag@CF, Inset the conductive Ag@CF. (d) Fabrication process of PDMS-based Ag@CF. (e) Large-area, ultraflexible and free-standing PDMS-based Ag@CF.

9. Application of lattice asymmetric all-solid-state supercapacitors

Figure S11a-c displays three lattice asymmetric all-solid-state supercapacitors (LASCs) connected in series to drive a LED, in which the LED was successfully lighted for more than 6 min (**Figure S11d-e**). Additionally, a self-powered nanosystem which was integrated by a triboelectric nanogenerator (TENG) and a LASC was shown in **Figure S11h**. Here, the TENG was used to harvest mechanical energy in contact-mode, and the detail description about the configuration of TENG can be found in **Figure S10**, ESI. Due to the output characteristic of alternating current from TENG (**Figure S11i**), a bridge rectification circuit was adopted. When a sinusoidal compression loading at 3.3 Hz was implemented on the TENG (**Figure S11j**), the charging curve of a LASC was obtained in **Figure S11k**, from which we can see that it can be charged to 90 mV within 11 min.

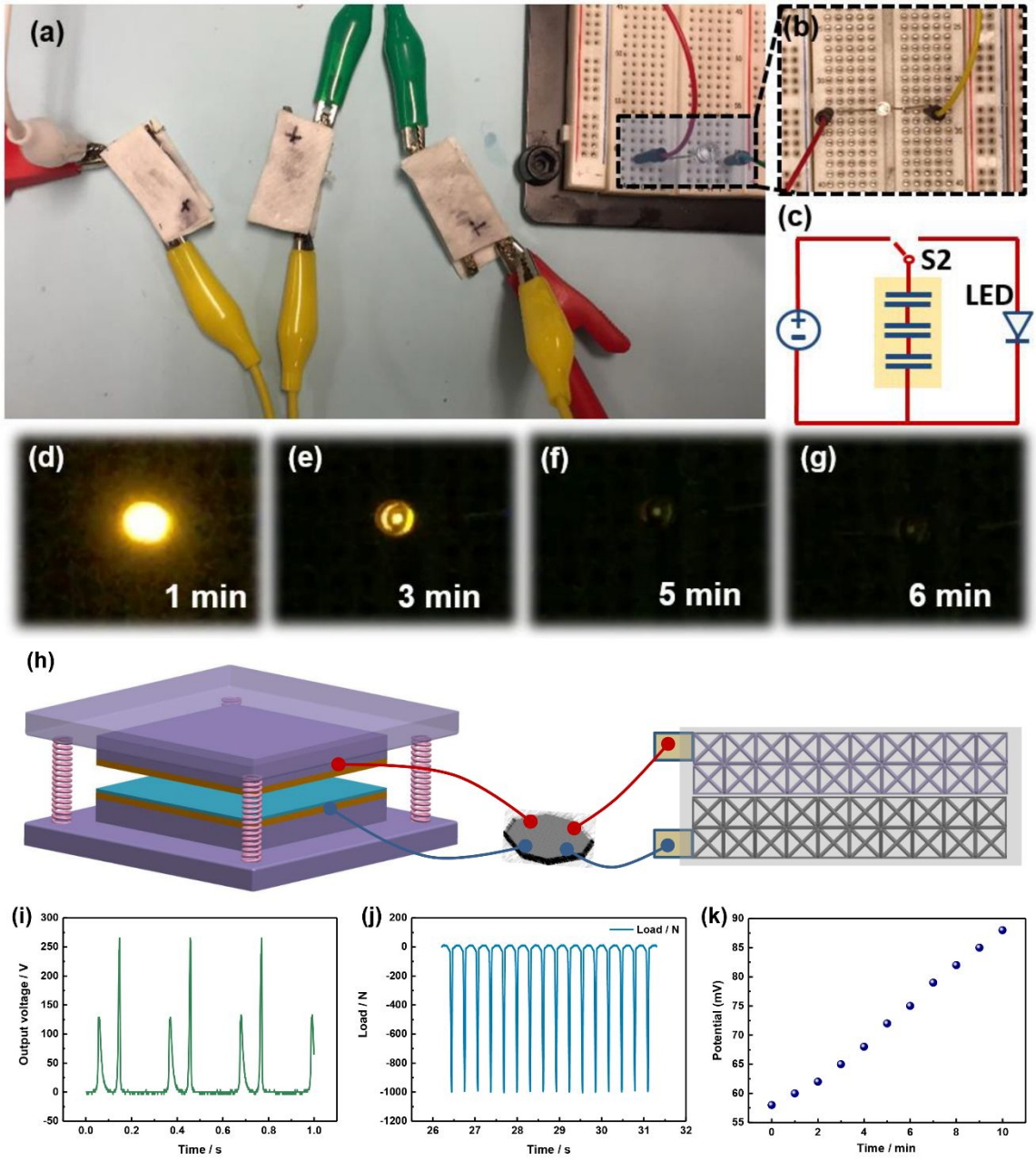

Figure S11. (a) Optical photograph of the as-fabricated device with three solid-state LASCs connected in series. (b) Magnified image of a LED. (c) Schematic diagram of the circuit. (d-g) Photographs of the LED at different lighting times. (h) Schematic diagram of the triboelectric nanogenerator charging the as-fabricated LASC. (i-k) Rectified output voltage vs. time curves generated by triboelectric nanogenerator,

load vs. time curve, and charging curves of supercapacitor charged by using the triboelectric nanogenerator.

Table S1 Comparison of specific capacitances of the other electrode materials and present work in a three-electrode system

Materials	Electrolyte concentration	Current density	Specific capacitance	Ref.
$CoNi_2S_4$/ Ni foam	6 M KOH	5 A g^{-1}	672 F g^{-1}	2
$NiCo_2S_4$/ Co_9S_8	6 M KOH	5 A g^{-1}	735 F g^{-1}	3
$CoNi_2S_4$/CNLDHs	6 M KOH	5 A g^{-1}	750 F g^{-1}	4
$CoNi_2S_4$	3 M KOH	5 A g^{-1}	702.3 F g^{-1}	5
Co-Ni sulfide	3 M KOH	5 A g^{-1}	1279 F g^{-1}	6
Ni-Co LDH/ rGO/ NF	6 M KOH	5 A g^{-1}	990 F g^{-1}	7
$CuCo_2S_4$/ rGO	3 M KOH	5 A g^{-1}	664.8 F g^{-1}	8
Ni-Co LDH/pen ink/CF	6 M KOH	5 A g^{-1}	910 F g^{-1}	9
Co_3O_4/ G/ Ni foam	6 M KOH	5 A g^{-1}	300 F g^{-1}	10
$CoNi_2S_4$/ G/ $MoSe_2$	6 M KOH	5 A g^{-1}	961 F g^{-1}	11
$CoNi_2S_4$/ MnO_2	6 M KOH	5 A g^{-1}	950 F g^{-1}	12
$CoNi_2S_4$/ Ni/ OTL	6 M KOH	5 A g^{-1}	1216 F g^{-1}	This work

where rGO, CNLDHs, is reduced graphene oxide. G is graphene, Co/Ni layered double hydroxides

Reference

(1) Stratasys. ABS-M30 for Fortus 3D Production Systems. *Stratasys Company Publications*: USA, **2008**.

(2) Pu, J.; Wang, T.; Wang, H.; Tong, Y.; Lu, C.; Kong, W.; Wang, Z. Direct Growth of $NiCo_2S_4$ Nanotube Arrays on Nickel Foam as High‐Performance Binder‐Free Electrodes for Supercapacitors. *ChemPlusChem* **2014,** *79,* 577-583.

(3) Hou, L.; Shi, Y.; Zhu, S.; Rehan, M.; Pang, G.; Zhang, X.; Yuan, C. Hollow Mesoporous Hetero-$NiCo_2S_4$/Co_9S_8 Submicro-Spindles: Unusual Formation and Excellent Pseudocapacitance Towards Hybrid Supercapacitors. *J. Mater. Chem. A* **2017,** *5,* 133-144.

(4) Tang, J.; Shen, J.; Li, N.; Ye, M. One-Pot Tertbutanol Assisted Solvothermal Synthesis of $CoNi_2S_4$/Reduced Graphene Oxide Nanocomposite for High-Performance Supercapacitors. *Ceram. Int.* **2015,** *41,* 6203-6211.

(5) Du, W.; Zhu, Z.; Wang, Y.; Liu, J.; Yang, W.; Qian, X.; Pang, H. One-Step Synthesis of $CoNi_2S_4$ Nanoparticles for Supercapacitor Electrodes. *Rsc Adv.* **2014,** *4,* 6998-7002.

(6) Li, X.; Li, Q.; Wu, Y.; Rui, M.; Zeng, H. Two-Dimensional, Porous Nickel–Cobalt Sulfide for High-Performance Asymmetric Supercapacitors. *ACS Appl. Mater. Inter.* **2015,** *7,* 19316-19323.

(7) Bai, X.; Liu, Q.; Zhang, H.; Liu, J.; Li, Z.; Jing, X.; Yuan, Y.; Liu, L.; Wang,

Nickel-Cobalt Layered Double Hydroxide Nanowires on Three Dimensional Graphene Nickel Foam for High Performance Asymmetric Supercapacitors. *J. Electrochim. Acta* **2016,** *215,* 492-499.

(8) Annamalai, K.; Tao, Y.-s. A Hierarchically Porous $CuCo_2S_4$/Graphene Composite as An Electrode Material for Supercapacitors. *New Carbon Mater.* **2016,** *31,* 336-342.

(9) Gao, L.; Utama, S. J.; Cao, K.; Zhang, H.; Li, P.; Xu, S.; Jiang, C.; Song, J.; Sun, D.; Lu, Y. Flexible Fiber-Shaped Supercapacitor Based on Nickel-Cobalt Double Hydroxide and Pen Ink Electrodes on Metallized Carbon Fiber. *ACS Appl. Mater. Inter.* **2017,** *9*, 5409-5418.

(10) Deng, X.; Li, J.; Zhu, S.; He, F.; He, C.; Liu, E.; Shi, C.; Li, Q.; Zhao, N. Metal–Organic Frameworks-Derived Honeycomb-Like Co_3O_4/Three-Dimensional Graphene Networks/Ni Foam Hybrid as A Binder-Free Electrode for Supercapacitors. *J. Alloy. Compd* **2017,** *693,* 16-24.

(11) Shen, J.; Wu, J.; Pei, L.; Rodrigues, M. T. F.; Zhang, Z.; Zhang, F.; Zhang, X.; Ajayan, P. M.; Ye, M. $CoNi_2S_4$ ‐ Graphene ‐ 2D ‐ $MoSe_2$ as An Advanced Electrode Material for Supercapacitors. *Adv. Energy Mater.* **2016,** *6,* 1600341.

(12) Yang, J.; Ma, M.; Sun, C.; Zhang, Y.; Huang, W.; Dong, X. Hybrid $NiCo_2S_4$@ MnO_2 Heterostructures for High-Performance Supercapacitor Electrodes. *J. Mater. Chem. A* **2015,** *3,* 1258-1264.